Lehigh University
Lehigh Preserve

Theses and Dissertations

2017

Roadway Marking Optics for Autonomous Vehicle Guidance and Other Machine Vision Applications

Anthony Thomas Konopka
Lehigh University

Follow this and additional works at: http://preserve.lehigh.edu/etd

 Part of the Electrical and Computer Engineering Commons

Recommended Citation
Konopka, Anthony Thomas, "Roadway Marking Optics for Autonomous Vehicle Guidance and Other Machine Vision Applications" (2017). *Theses and Dissertations*. 2669.
http://preserve.lehigh.edu/etd/2669

This Thesis is brought to you for free and open access by Lehigh Preserve. It has been accepted for inclusion in Theses and Dissertations by an authorized administrator of Lehigh Preserve. For more information, please contact preserve@lehigh.edu.

Roadway Marking Optics for Autonomous Vehicle Guidance and Other Machine Vision Applications

by

Anthony T. Konopka

A Thesis

Presented to the Graduate and Research Committee

of Lehigh University

in Candidacy for the Degree of

Master of Science

in

Electrical Engineering

Lehigh University

May 2017

Copyright

Certificate of Approval

This thesis is accepted and approved in partial fulfillment of the requirements for the Master of Science.

May 4, 2017

Date

Douglas Frey

Thesis Advisor

William Haller

Co-Advisor

Svetlana Tatic-Lucic

Chairperson of Department

Acknowledgements

The author wishes to thank William R. Haller of LimnTech Scientific Inc., whose shared knowledge, guidance, and advice were invaluable throughout the course of this work. His support, along with the support of LimnTech Scientific Inc., was tremendously appreciated.

The author additionally wishes to thank Douglas D. Dolinar of Guidemark Inc., whose industry knowledge and expertise were incredibly helpful assets. The support and assistance provided by Professor Douglas R. Frey of Lehigh University is also greatly appreciated. The author further wishes to express gratitude to Lehigh University and its donors for the financial support which made this graduate study possible.

Table of Contents

List of Tables

List of Figures

Abstract

This work determines optimal planar geometric light source and optical imager configurations and electromagnetic wavelengths for maximizing the reflected signal intensity when using machine vision technology to image roadway markings with embedded spherical glass beads. It is found through a first set of experiments that roadway marking samples exhibiting little or no bead rolling effects are uniformly reflective with respect to the azimuthal angle of observation when measured for retroreflectivity within industry standard 30-meter geometry. A second set of experiments indicate that white roadway markings exhibit higher reflectivity throughout the visible spectrum than yellow roadway markings. A roadway marking optical model capable of being used to determine optimal geometric light source and optical imager configurations for maximizing the reflected signal intensities of roadway marking targets is constructed and simulated using optical engineering software. It is found through a third set of experiments that high signal intensities can be measured when the polar angles of the light source and optical imager along a plane normal to a roadway marking are equal, with the maximum signal intensity being measured when the polar angles of both the light source and optical imager are 90°.

1. Introduction

Machine vision technology is rapidly becoming an integral part of modern-day automotive transportation systems. In addition to general autonomous vehicle guidance, machine vision technology plays a critical role in lane departure warning systems (LDWS), adaptive cruise control systems (ACCS), lane keeping systems, and lane change assist systems currently implemented in many motor vehicles. Applications for the technology in automated GPS-based line striping systems and other systems related to roadway construction and maintenance are currently in development as well. The increasing importance of machine vision technology to automotive transportation and associated applications cannot be understated [1].

A machine vision system is any system which incorporates imaging-based inspection and analysis in order to perform tasks such as automatic inspection, process control, or robot guidance. Such systems typically consist of a light source (which may be a passive source, such as sunlight, or an active source, such as a powered light emitter), a target, an optical imager (which may be a camera, lidar system, or other device) for receiving reflected energy from the target, and a computer for processing the acquired images using appropriate image processing software. Machine vision systems are somewhat analogous to the biological vision systems that humans use to view their surroundings, where their eyes act as optical imagers and image processing is performed by the brain. A schematic illustration of a machine vision system for imaging roadway markings is shown in Figure 1.

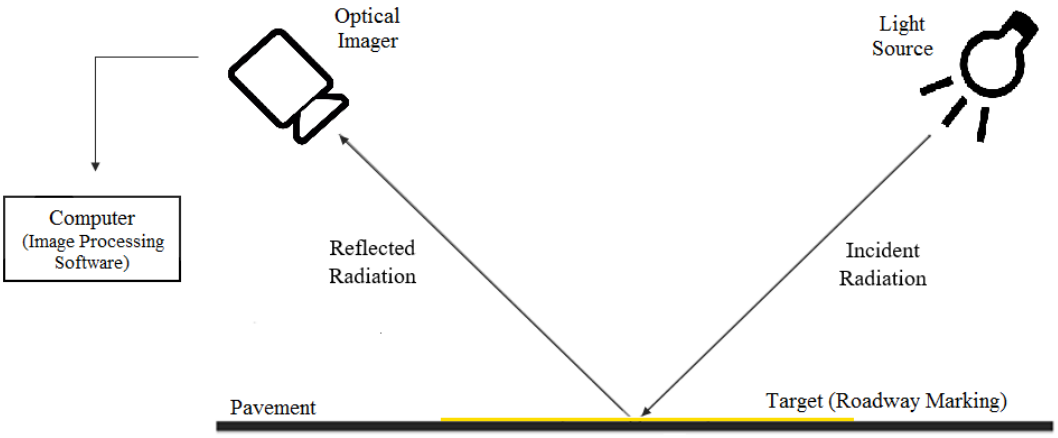

Figure 1: Schematic diagram of machine vision system for imaging roadway markings.

In order to function correctly, the aforementioned automotive transportation-related systems typically require a mechanism to detect various roadway elements such as other vehicles, pedestrians, or roadway markings. This functionality is typically provided by machine vision technology capable of optically imaging and processing the images of some or all of these roadway elements. The processed images produced by machine vision systems may then be used to determine the positions of the roadway elements with respect to the vehicle so that the overall system can respond accordingly. Such a process is employed, for example, when a lane keeping system sends a warning to a vehicle operator after detecting that their vehicle has drifted out of its lane.

While there are still many problems to be solved in relation to detection of every one of these roadway elements, the focus of this work is placed on several of the

problems associated with the detection of roadway markings. Machine vision technology capable of accurately and reliably imaging roadway markings is a crucial component of many transportation-related systems. The aforementioned lane keeping system, for example, must be capable of accurately determining the positions of roadway markings in relation to the vehicle in order to function correctly. High levels of accuracy and reliability have yet to be achieved however, as many modern systems struggle to image roadway markings in environmental conditions such as rain, fog, haze, night, or other conditions that decrease optical visibility. Additionally, there is still a need for higher roadway marking detection reliability even when optically-limiting environmental conditions are not present [1]. Further optical study of roadway markings is therefore prudent so that manufacturers of machine vision systems, roadway marking materials, and other related technologies are able to adapt their products in order to improve the reliability of roadway machine vision applications.

The specific focus of this work is the determination of optimal geometric configurations and electromagnetic wavelengths for maximizing the reflected signal intensity when imaging roadway markings with machine vision technology. While many previous studies have addressed problems related to the maximization of roadway marking visibility for vehicle operators [2] [3] [4], few studies have addressed the unique problems associated with the use of roadway markings as machine vision targets. When the optical properties of roadway markings are considered and machine vision system components are adjusted accordingly, the reflected signal intensity measured from roadway marking targets can be significantly increased. This is a highly desirable result,

as a high reflected signal intensity will increase the efficacy of the software used to process the captured images, thereby increasing the detection reliability of the overall machine vision system.

Section 2 of this work contains general background information about roadway markings intended to contextualize discussions regarding roadway markings as targets for machine vision systems. This information is used to formally define the problem statement included in Section 3, followed by mathematical definitions and derivations that establish a theoretical basis for the optical and electromagnetic properties of roadway markings in Section 4.

Section 5 describes the first set of experiments in this work, including a description of a set of azimuthal angular dependence experiments performed in order to gain a sufficient understanding of the optical characteristics of roadway markings for the purpose of constructing an optical model of the machine vision target. A description of a set of roadway marking binder reflectivity experiments that explore how the optical response of roadway markings vary with the emitted wavelengths of the light source in a machine vision system is then given in Section 6, with Section 7 including details regarding the optical roadway marking model constructed using optical engineering software. Section 7 also includes simulation results detailing the model's theoretical response to various machine vision system geometric configurations. A description of a set of machine vision imaging experiments performed in order to confirm the theoretical geometric results obtained from the optical model is finally given in Section 8.

2. Background

A brief overview of currently accepted knowledge regarding roadway marking material is contained in the following sections. This information is included in order to contextualize discussion of roadway markings as targets for machine vision systems. Formal definitions and standard measurement practices for optical concepts relating to roadway markings are included in order to further clarify the discussion.

2.1. Roadway Markings

In its Manual on Uniform Traffic Control Devices (MUTCD), the United States Department of Transportation (USDOT) categorizes roadway markings as traffic control devices. Markings that fall into this category include center lines, lane lines, edge lines, approaches to obstructions, stop and crosswalk lines, and various word and symbol markings. Typical colors for roadway markings include white and yellow [5]. Several example drawings of roadway markings that would need to be detected by various machine visions systems are included in Figure 2 (modified from [5]).

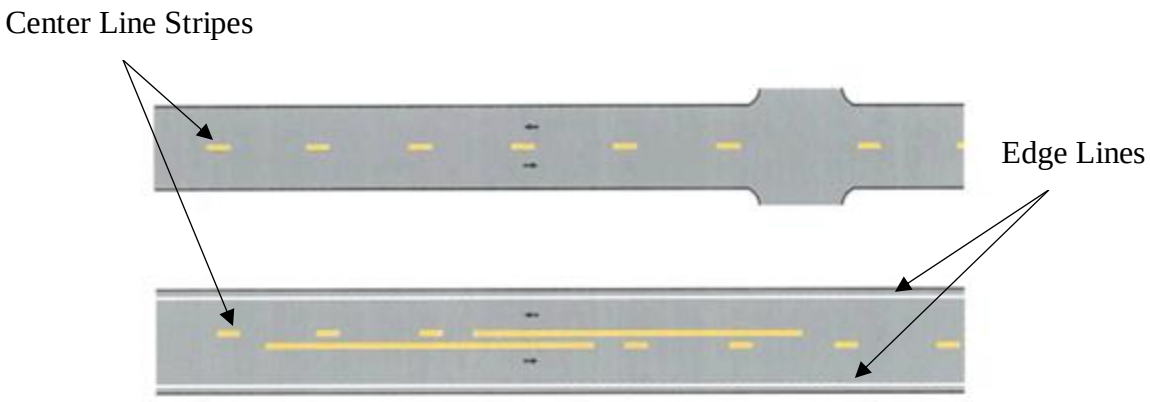

Figure 2: Two-lane roadway marking drawing.

USDOT specifications state that the base materials used to establish roadway markings may be paint, epoxy, or thermoplastic materials, with several other materials being acceptable as well. These materials will typically include white or yellow pigmentation so that the roadway markings will exhibit proper colorization, as well as binding compounds intended to increase the adherence of the materials [5]. Due to the presence of the binding compounds, these materials are typically referred to as “binders” in the roadway marking industry. Table 1 includes statistics on the types of binders likely to be imaged by machine vision systems in the United States [6]. The experiments described in this work are conducted using paint and epoxy roadway marking samples.

Table 1: Typical Roadway Marking Binders Used in the United States

Pavement Marking Material	Percentage of Lane Miles
Conventional Paints	58
Thermoplastics	21
Epoxies	6
Tapes	5
Polyesters	2
Profiled Thermoplastics	2
Other	6

Roadway markings are typically applied by specially designed vehicles with built-in carriages customized to apply a specific type of roadway marking material, as shown in Figure 3. The binder (paint, in the case of Figure 3) application is typically followed by an application of small, optically transmissive glass beads which become embedded in the binder and modify the optical properties of the roadway markings to increase the visibility of the markings to human vehicle operators in otherwise low visibility conditions. The use of glass beads in this fashion has a long history and has become a commonly accepted practice worldwide [7].

Figure 3: Typical roadway marking paint truck (left) with magnified view of carriage (right).

A typical bead gun applicator spraying glass beads onto one half of a yellow center line is shown in Figure 4 [8]. Bead gun applicators are typically mounted on the roadway marking vehicle carriage close to the binder applicators. Also shown in Figure 4 is a magnified image of a yellow roadway marking binder with embedded glass beads, where multiple sizes of beads are present at various different embedment levels within the binder [8]. As previously discussed, the presence of the embedded glass beads significantly improves the overall optical properties of the roadway markings. This work includes studies of the optical effects of these embedded glass beads so that machine vision technology can more reliably image roadway markings.

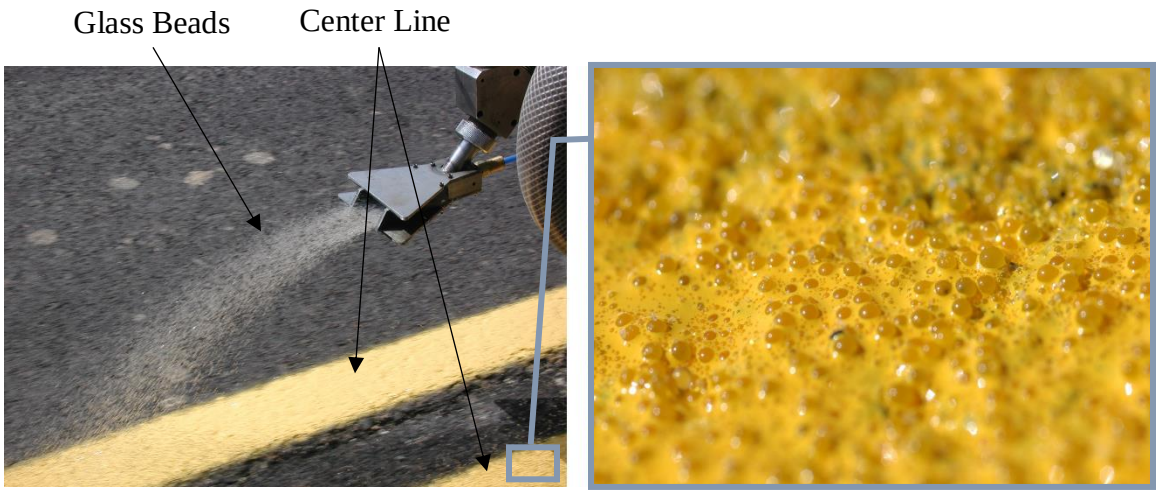

Figure 4: Bead gun applicator (left) and magnified roadway marking binder with embedded glass beads (right)

2.2. Retroreflection

An understanding of the optical properties of roadway markings is critically relevant to the design of any machine vision system intended to image roadway markings. As such, the optical consequences of embedding glass beads into roadway markings must be understood. As previously discussed, the purpose of embedding glass beads into roadway markings is to change the overall optical properties of the composite (binder with embedded glass beads) material. Specifically, the addition of the glass beads is intended to produce retroreflections when visible light is made to be incident on a roadway marking from a certain specific geometry. A retroreflection is defined as a type of reflection where the reflected light is returned preferentially in the directions closest to the opposite of the direction of the incident light as shown in Figure 5.

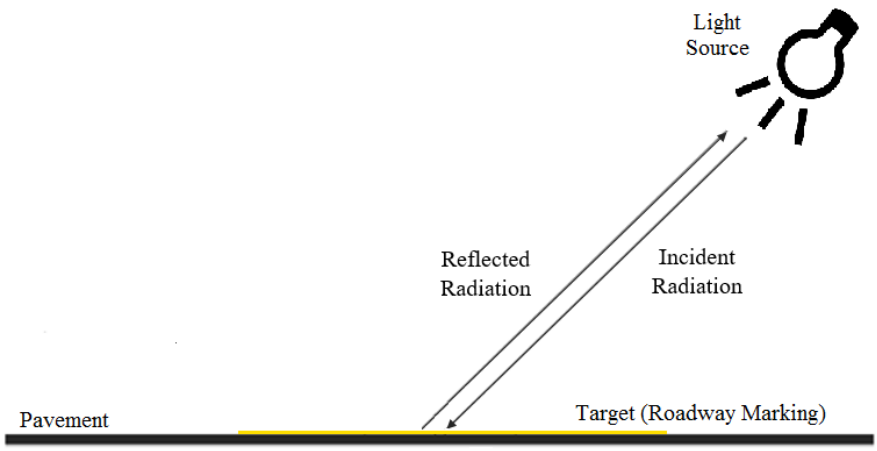

Figure 5: Roadway marking retroreflection diagram.

The specific geometry at which roadway markings must produce retroreflections is defined for the purposes of evaluating roadway marking quality by the European Committee for Standardization (CEN) [9]. Their standards describe a specific measurement geometry that includes a light source (to simulate a vehicle headlight), a retroreflector (the pavement marking), and a light receiver (to simulate the eyes of a vehicle operator). The geometry is specifically chosen to simulate the angle at which a vehicle operator would most likely observe the light from their vehicle headlights after it has been retroreflected off of the roadway marking when the vehicle is approximately 30 meters away from the marking [10]. The geometry is therefore referred to as "standard 30-meter geometry" and is shown as specified in a diagram in terms of an observation angle (α) and entrance angle (β) in Figure 6 (adapted from [10]).

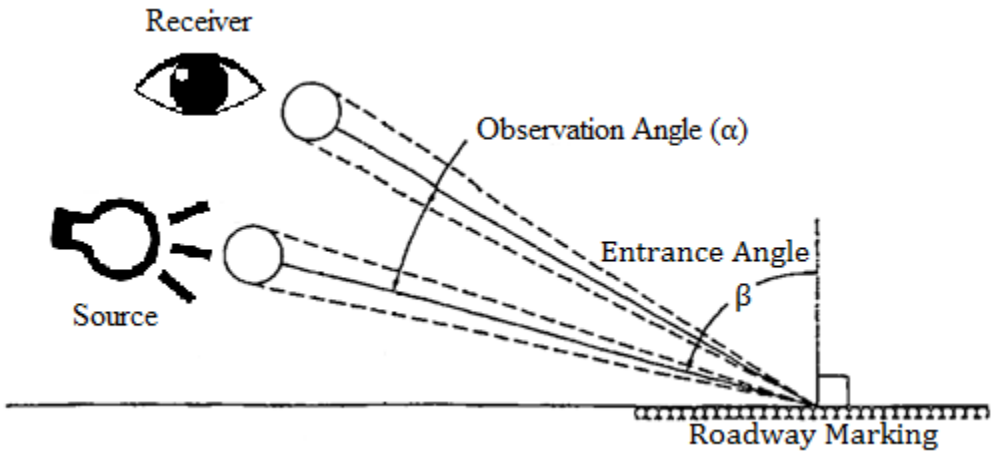

Figure 6: Standard 30-meter geometry diagram.

The CEN specifies an entrance angle of 88.76 ± 0.02° and an observation angle of 1.05 ± 0.02°. These angles were determined to correspond to a viewing distance of approximately 30 meters, with the light source height being approximately 0.65 meters and the light receiver height being approximately 1.2 meters [10].

The ability of a given roadway marking to produce retroreflections within a 30-meter geometry can be measured using a retroreflectometer (such as the retroreflectometer used in several of the experiments involved with this work, as described in Section 5). A retroreflectometer is capable of measuring a material's coefficient of retroreflected luminance (R_L), which is a formal measure of the material's retroreflectivity (ability to produce retroreflections) within 30-meter geometry [11].

In the context of roadway markings, the coefficient of retroreflected luminance is formally defined as the ratio of the luminance (L) of the reflected radiation to the illuminance (W) at the surface of the roadway marking due to the incident radiation as shown in Equation 1. Luminance is defined as the luminous intensity per unit area of light traveling in a given direction (typically expressed in candelas per square meter) and illuminance is defined as the total luminous flux incident on a surface (typically expressed in candelas per square meter per steradian). The typical units of expression for the coefficient of retroreflected luminance can therefore be simplified to steradians^{-1} [12].

$$R_L = \frac{L}{W} \qquad (1)$$

A typical roadway marking retroreflectometer (such as the one used in the experiments described in Section 5) will measure the coefficient of retroreflected luminance within the visible spectrum. Specifically, the values measured by a retroreflectometer will be a weighted average value, with the weighting being done according to the luminosity function, which describes the average spectral sensitivity of the human eye to wavelengths spanning the visible spectrum [10]. All retroreflectivity values included in this work were measured in the described fashion. Values measured using other types of optical imagers (such as the digital illuminance meter and digital camera optical imagers used in the experiments described in Section 6 and Section 8 respectively) are weighted according to the spectral sensitivity curves of each particular device.

2.3. Bead-Binder Composite Material

In order to further illustrate the mechanism by which an embedded glass bead is able to retroreflect incident radiation in a 30-meter geometry system, a magnified diagram of an embedded glass bead is shown in Figure 7 [13]. The incoming light from the light source is refracted down towards the binder material (point A), where it is subsequently reflected within the glass bead (point B) and refracted back towards the light receiver (point C). The extent to which this mechanism occurs is partially dependent upon the size, refractive index, roundness, and clarity of the glass beads, as well as several other factors [14].

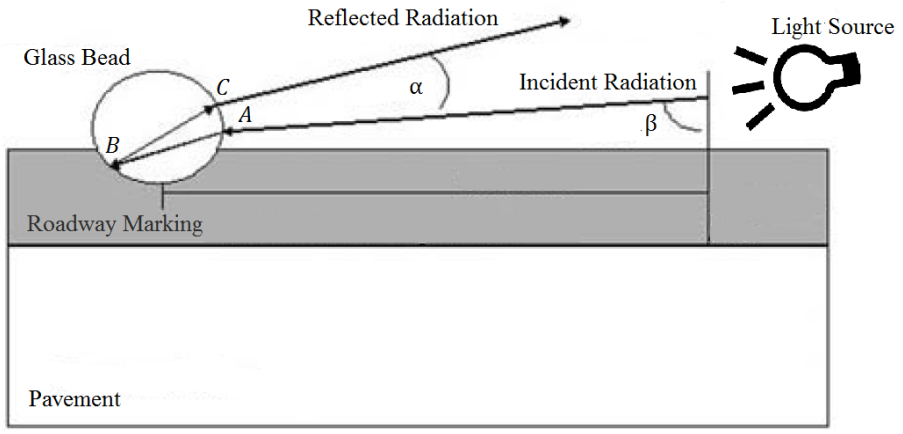

Figure 7: Embedded glass bead retroreflection diagram.

The cumulative effect of each glass bead redirecting light in the described fashion results in a relatively large of amount of retroreflection from the composite roadway marking. This effect is demonstrated in Figure 8, where the roadway marking sample with embedded glass beads exhibits significantly higher contrast with respect to the surrounding surface when a light source is applied. A critical goal of any machine vision system is to capture images with high contrast between the target and other materials in the image, so an understanding of the mechanisms that create these retroreflective effects in roadway markings is a key component of this work.

Figure 8: Epoxy roadway marking without glass beads (left) and with glass beads (right).

USDOT regulations recognize that the optimal bead embedment level to maximize retroreflectivity (for standard 30-meter geometry) is such that 50% of the bead is embedded in the binder material and 50% of the bead is exposed above the binder material as approximately shown in Figure 7. Bead application rates are therefore specified by legal entities according to the type of binder and the dimensions of the beads in order to produce a bead density that maximizes the proportion of the beads that are optimally embedded [15]. As such, all roadway marking samples used in the experiments described in this work were applied at USDOT specified application rates in order to ensure that all obtained results would match those that would be obtained from regular roadway markings.

As previously discussed, the extent to which roadway markings produce retroreflections is partially dependent upon the physical dimensions of their embedded glass beads. Specifications regarding glass bead dimensions are typically determined by local municipalities and may vary depending on the jurisdiction in which a given roadway marking is located. As all roadway marking samples used in the experiments

described in this work according to specifications set by the Pennsylvania Department of Transportation (PennDOT), PennDOT glass bead specifications are included in this section for reference purposes [16].

PennDOT specifications classify groups of glass beads into one of four categories (Type A, Type B, Type C, or Type D) according to the distribution of diameters within a sample of each group of glass beads. The four distributions are approximately summarized in Figure 9, where all percentages are by weight of the sample [16]. The glass beads dispensed onto the samples used in the experiments described in this work are all classified as either Type A or Type B.

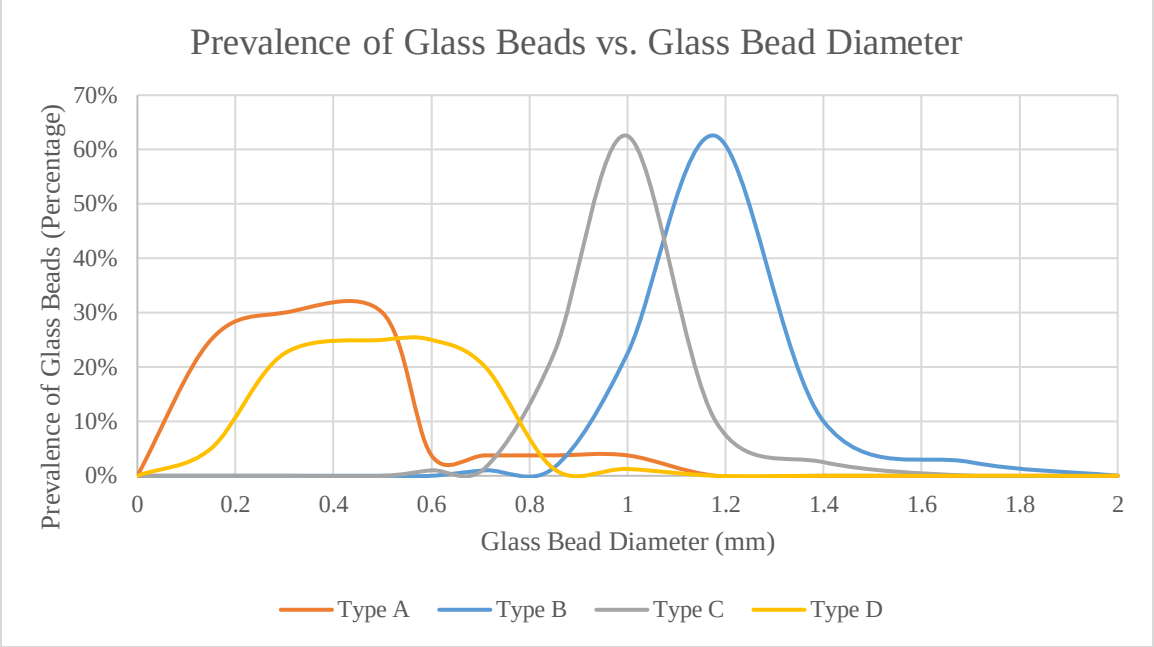

Figure 9: PennDOT glass bead diameter distribution specifications for various glass bead types.

Specifications for the types of glass beads applied to specific roadway marking binders are typically set by local municipalities entities and may vary between jurisdictions. For reference purposes, Table 2 includes PennDOT glass bead type specifications for several common roadway marking binders (paints [17], epoxies [18], and thermoplastics [19]). Paint and epoxy samples were used in the experiments described in this work.

Table 2: PennDOT Glass Bead Type Specifications for Select Roadway Marking Binders

Roadway Marking Binder	Glass Bead Types
Paints	Type A
Epoxies	Type A + Type B
Thermoplastics	Type A

A typical refractive index at optical wavelengths for ordinary glass beads is 1.5 (manufacturers typically specify a range of 1.5 to 1.55). “High index” glass beads typically have a refractive index of approximately 1.9 and “super high index” glass beads typically have refractive indexes of approximately 2.3 or higher. A larger refractive index generally leads to greater refraction within the glass bead and, as a result, higher retroreflectivity for the aggregate roadway marking. However, as high index and super high index glass beads are typically more expensive to manufacture, the vast majority of roadway markings are embedded with ordinary glass beads [20]. Similarly, only ordinary glass beads were dispensed onto the samples used in the experiments described in this work.

2.4. Bead Rolling Effects

As previously described, glass beads are typically deposited onto the freshly applied binder from a dispensing nozzle mounted on the same vehicle that was used to apply the binder. If glass beads were to be simply dropped from the moving vehicle, this would give the beads a non-zero horizontal velocity as they collide with the binder. The beads would then roll through the binder before becoming embedded, accumulating a coating of extra binder material and covering each bead with more material than desired, thus inhibiting the typical reflective mechanism facilitated by the beads as illustrated in Figure 10 (adapted from [21]). This bead rolling greatly reduces the retroreflectivity of the applied roadway marking, resulting in lower visibility for vehicle operators. This is highly undesirable for autonomous vehicle systems as well, as low or inconsistent reflective properties are not conducive to reliable machine vision imaging [22].

To counteract this effect, many roadway line striping vehicles will make use of a directional bead gun nozzle mechanism to dispense the glass beads. The bead gun nozzle is pointed in the direction directly opposite the direction of vehicle motion and attempts are made to dispense the beads with a horizontal velocity exactly matching that of the truck (except in the opposite direction). Ideally, this should allow the opposing horizontal velocity components of the beads to approximately cancel, resulting in a “zero-velocity” bead drop where the bead simply drops directly downwards onto the binder with symmetrical embedment [22].

The ideal result of this methodology is shown in a diagram in Figure 10 (adapted from [21]). Figure 10a shows a glass bead being dispensed onto a binder from a moving vehicle without any compensation. The bead enters the binder with a non-zero horizontal velocity, leading to additional binder coverage as shown in Figure 10b. This coverage would prevent some incident radiation from entering the bead and being retroreflected. In contrast, Figure 10c shows a glass bead being dispensed using a zero-velocity bead drop methodology. The bead enters the binder with zero horizontal velocity, resulting in normal bead embedment as shown in Figure 10d.

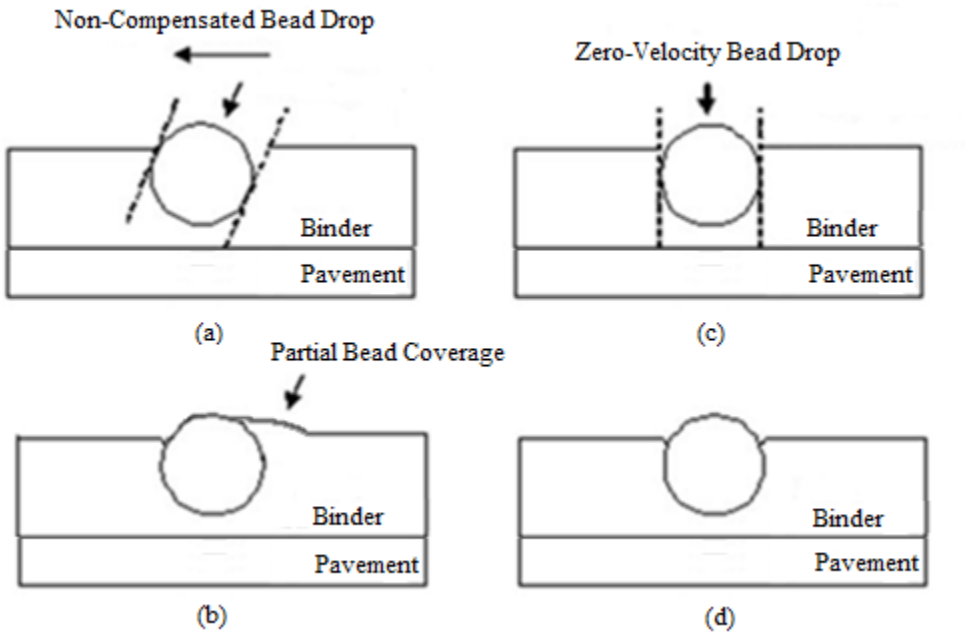

Figure 10: Glass bead horizontal velocity embedment effects for non-compensated bead drop (left) and zero-velocity bead drop (right).

Various efforts have been made to study and evaluate the presence of bead rolling effects in the roadway markings applied to roadways. One such study [21] in North Carolina performed statistical analysis on a series of retroreflectivity measurements taken on various painted highway roadway markings. In each sample area, multiple retroreflectivity measurements were taken in the direction of the application of the roadway marking and compared with multiple retroreflectivity measurements taken in the opposite direction. Both data sets are then compared using a statistical T-test in order to determine if there was a statistically significant difference between measurements taken in each direction. A statistical difference would indicate the presence of bead rolling effects in the roadway markings. A T-test is similarly used in this work to analyze experimental data as described in Section 5.

The North Carolina study found that there was indeed a statistically significant difference between the retroreflectivity measurements taken in the two opposing directions, but that the difference became less significant as the roadway markings were subjected to additional aging [21]. This result suggests that while bead rolling effects may be present in newly applied roadway markings that were not applied with a zero-velocity bead drop methodology, these effects should significantly diminish as the upper layer of the roadway marking binder wears away over time.

All samples used in the experiments described in this work were therefore applied using a directional bead gun nozzle mechanism in order to minimize bead rolling effects. Additional special attention was given to bead rolling effects in the experiments described in Section 5, where a handcart applicator was used in place of a bead gun in

order to produce control samples that were guaranteed to be devoid of bead rolling effects. This was an important consideration because, as the North Carolina study indicates, bead rolling effects are not present in a majority of the roadway markings a machine vision-based system would likely encounter in the field [21]. The samples were thus applied in order to mimic typical roadway markings.

3. Problem Statement

As described in Section 1, this work specifically focuses on the determination of optimal planar geometric light source and optical imager configurations and electromagnetic wavelengths for maximizing the reflected signal intensity when using machine vision technology to image roadway markings with embedded spherical glass beads. A spherical coordinate system is used for the purposes of specifying geometric configurations and positions in this work, as shown in Figure 11, unless otherwise noted. The figure demonstrations coordinate notation where positions are defined by their radial distance (r), polar angle (θ), and azimuthal angle (φ) as referenced to the origin, which is defined to be on the surface of a given roadway marking stripe residing in the x-y plane.

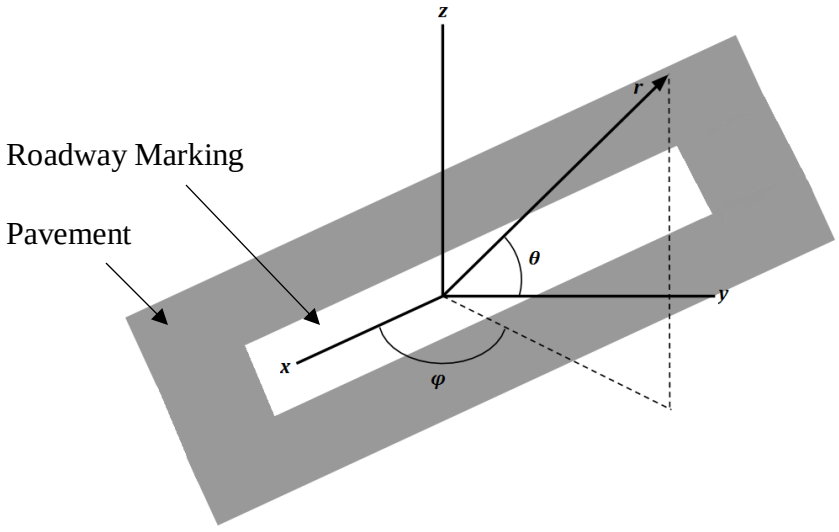

Figure 11: Spherical coordinate system diagram with origin defined on the surface of a roadway marking.

The specific objectives of this work are as follows:

- Perform a set of azimuthal angular dependence experiments to determine the extent to which reflection properties of roadway markings (with and without glass beads) change with respect to the azimuthal angle (φ) of observation;

- Perform a set of binder reflectivity experiments to determine the extent to which reflective properties of roadway marking binders (without glass beads) change with respect to the incident electromagnetic wavelength;

- Use the data measured in the azimuthal angular dependence and binder reflectivity experiments to generate a planar optical ball lens model for simulating the reflective mechanism formed by the interfaces between roadway marking binders and embedded glass beads in order to determine planar light source and imager positional polar angle (θ) configurations for maximizing observed reflectivity of roadway markings; and

- Perform a set of machine vision imaging experiments where the polar angular positions of the imager and light source components of a machine vision system are varied and the measured reflected light intensity from a roadway marking target (with glass beads) is recorded in order to confirm the reflectivity data obtained from the planar optical model.

4. Theoretical Foundations

Derivations and formal definitions of several electromagnetic and optical phenomena relevant to the electromagnetic properties of roadway markings are included in the following sections. These definitions are included in order to establish a theoretical foundation for the reflection effects observed in the experiments described in this work. The equations derived in the following sections can be used to model the propagation of electromagnetic radiation that is incident on any generic roadway marking with embedded glass beads. When coupled with the experimental findings detailed in Section 5 and Section 6, these equations can be used to create the simulation model detailed in Section 7.

Geometric optical modeling, where rays are used as an abstraction to approximate the paths along which electromagnetic plane waves propagate, is used throughout this work. The simplifying assumptions of these models are that light rays propagate in rectilinear paths as they travel in homogeneous media, follow curved paths in media in which the refractive index changes, and may be absorbed or reflected [23].

Geometric optical modeling is used in place of diffraction (or physical) optical modeling in this work, resulting in models that neglect electromagnetic diffraction effects. This choice is made due to the physical characteristics of the optical systems discussed in this work. Diffraction effects occur as a result of the fact that real-world electromagnetic waves travel in the form of wavefronts, where waves with a common origin travel along certain mathematically-defined surfaces while their phases stay

simultaneous at any given instant of time. According to the Huygens-Fresnel Principle, every unobstructed point of a wavefront (at a given instant of time) serves as a source of spherical secondary wavelets which propagate at the same frequencies as that of the primary wave. Diffraction effects can therefore be thought of as deviations from the geometric wave model that occur due to the fact that the amplitudes of the resulting electromagnetic fields are actually superpositions of the described wavelets [23].

Typical roadway marking glass bead diameters can range from 2.0 millimeters to 150 micrometers (as described in PennDOT standards) [16], while the electromagnetic wavelengths corresponding to the visible spectrum light used in this work can range from 390 nanometers to 700 nanometers [24]. The resulting optical systems therefore contain apertures that are approximately 1000 times larger than the relevant electromagnetic wavelengths. As the electromagnetic field amplitude variations resulting from diffraction effects will therefore be miniscule on the geometric scale used in this work, the diffraction effects associated with these optical systems are assumed to be negligible.

4.1. Bead-Binder Interfaces

In regards to roadway markings, electromagnetic interfaces exist at the boundaries between each glass bead and the roadway marking binder, between each glass bead and the surrounding air, and between the air and the roadway marking binder. Formally, an electromagnetic interface is formed at any boundary between two material regions (Region 1 and Region 2) of differing refractive indices (n_1 and n_2 respectively) as

generically shown in Figure 12, where the refractive index of a material is the ratio of the phase velocity of light through the material (v_p) to the phase velocity of light in a vacuum (c) as shown in Equation 2 [23].

$$n = \frac{c}{v_p} \tag{2}$$

A light ray propagating through Region 1 and incident on any electromagnetic interface will result in the formation of a reflected ray (which propagates away from the interface through Region 1) and a transmitted ray (which propagates away from the interface through Region 2). A generic two dimensional cross-sectional diagram of this situation is shown in Figure 12, with the angles of incidence (θ_i, θ_r, and θ_t) of the light rays (incident, reflected, and transmitted respectively) being indicated with respect to the axis normal to the interface. Points A, B, C, and O are included for reference purposes. Also included are a set of possible directions for the electric fields associated with the incident, reflected, and transmitted rays (E_i, E_r, and E_t respectively).

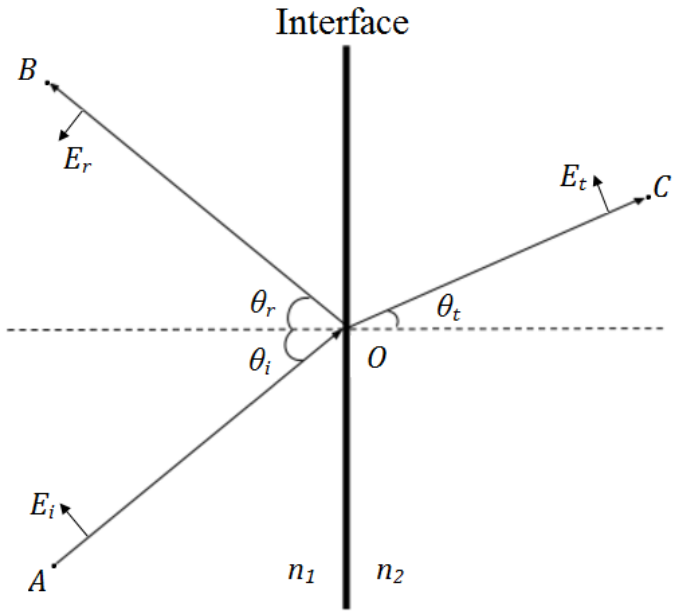

Figure 12: Generic electromagnetic interface diagram with rays representing plane waves.

The angular relationships between the incident ray and the reflected ray are determined according to the Law of Reflection (as shown in Equation 3), and the angular relationships between the incident ray and the transmitted ray are determined according to Snell's Law (as shown in Equation 4). These relationships are used in Section 4.2 to derive equations associated with the propagation of electromagnetic radiation through spherical glass beads so that the reflective properties of roadway markings can be properly modeled.

$$n \sin \theta_i = n \sin \theta_r \tag{3}$$

$$\theta_i = \theta_r \tag{4}$$

Additionally, it is important to develop the capability to determine the proportion of the energy associated with an incident ray becomes associated with the corresponding reflected ray and what proportion of the energy becomes associated with the corresponding transmitted ray. Reflected signal intensity in a machine vision system is directly proportional to the amount of energy that reaches the optical imager.

The energy associated with the reflected ray is determined according to the reflectance (R) of the interface, which is a ratio of electric field intensities associated with the reflected and incident electric fields ($E_{0,r}$ and $E_{0,i}$ respectively) as shown for normal incidence in Equation 5.

$$R = \left(\frac{E_{0,r}}{E_{0,i}}\right) = \left|\frac{n_1 - n_2}{n_1 + n_2}\right|^2 \qquad (5)$$

The energy associated with the transmitted ray is similarly determined according to the transmittance (T) of the interface, which is a ratio of electric field intensities associated with the transmitted and incident rays ($E_{0,t}$ and $E_{0,i}$ respectively) as shown for normal incidence in Equation 6.

$$T = \left(\frac{E_{0,t}}{E_{0,i}}\right) = 1 - R = 1 - \left|\frac{n_1 - n_2}{n_1 + n_2}\right|^2 \qquad (6)$$

Formal derivations of these relationships (as well as formal definitions for various related concepts) are included in Appendix A.

4.2. Lensmaker's Equation

The electromagnetic interfaces associated with roadway markings are, of course, not uniformly flat (as assumed in the model detailed in Section 4.1). Rather, the glass beads embedded in roadway marking binders form many curved interfaces along the otherwise approximately flat roadway marking surface. Through the use of the lensmaker's equation (derived in this section), the optical properties of the aggregate roadway marking can therefore be modeled as a superposition of the transmitted and reflected light rays resulting from the interactions between incident light rays and each individual set of interfaces on the roadway marking.

The described overall model requires some additional modeling of the curved interfaces formed by the glass beads. As the glass beads are highly transmissive ($T \approx 0.96$ for normally incident light on glass beads with $n = 1.5$), a thick lens model may be used for this purpose. A lens is defined as an optically transmissive device which affects the focus of a light beam through refractive mechanisms.

A cross-sectional diagram of a typical thick lens model is shown in Figure 13, with the thickness of the lens (d) and radii of curvature (r_1 and r_2) for each refracting surface being indicated in the figure. Points A, B, C, D, E, and F are included for reference purposes. Reflected and transmitted rays are shown at the interfaces formed at

points B and C, with the majority of the energy originally associated with the incident ray ($\overline{AB}$) being associated with the transmitted rays ($\overline{BC}$ and $\overline{CD}$) rather than the reflected rays ($\overline{BE}$ and $\overline{CF}$). Also included in the figure are lengths h_i and h_t, which correspond to the lateral distances from each respective radii of curvature for the first incident and final transmitted rays respectively. Incident (θ_i) and transmitted (θ_t) ray angles are also respectively included.

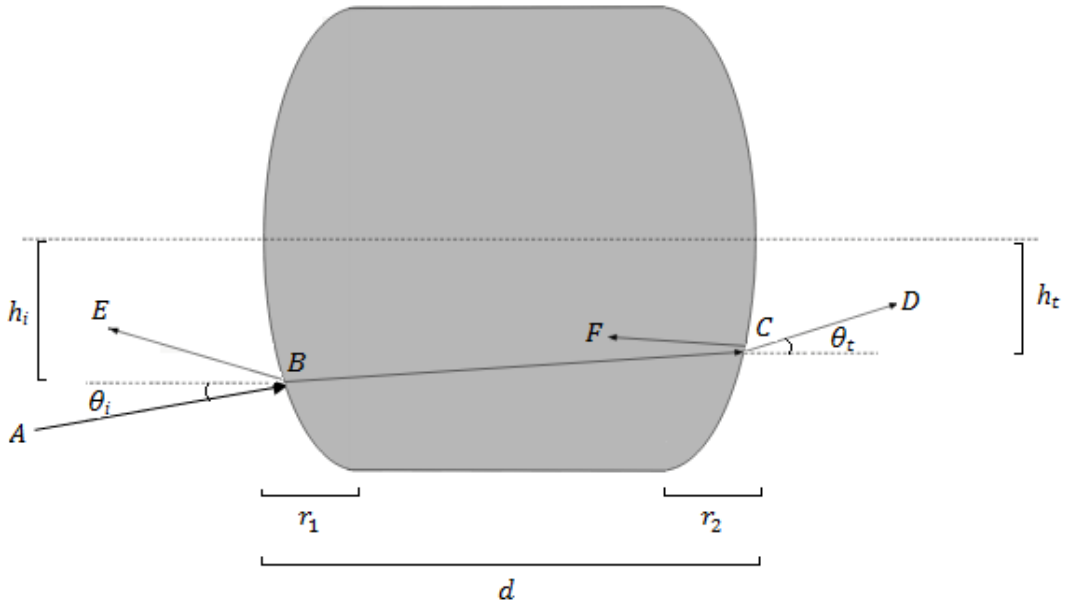

Figure 13: Thick lens cross-sectional diagram.

In the discussion of lenses, it is often convenient to refer to the dioptric power ($\mathcal{D}$) of each refracting surface of the lens. Dioptric power is the reciprocal of the focal

distance (f) of a refracting surface (which defines the distance from the surface at which all transmitted light rays will converge, regardless of their incident angles), and is related to the surface's radius of curvature and the refractive index of the lens as shown in Equation 7 (assuming the lens is located in air where $n_0 = 1$). This relationship will be used in the derivation of the lensmaker's equation.

$$\mathcal{D} = \frac{1}{f} = \frac{n-1}{r} \tag{7}$$

Any incident ray on a refracting surface can be described in terms of its incident angle (θ_i) and its lateral distance from the center of curvature of the refracting surface (h_i). The dioptric power of the refracting surface can be used to relate the angle of the incident ray to the angle of the transmitted ray (θ_t) as shown in Equation 8, where n_1 and n_2 are the refractive indices in which the incident and transmitted rays are respectively traveling [23].

$$n_2\theta_t = n_1\theta_i - h_i\mathcal{D} \tag{8}$$

After noting that the lateral distance from the center of curvature of the refracting surface does not change across an interface ($h_i = h_t$, where h_t is the corresponding distance for the transmitted ray), Equation 8 can be expressed in matrix form as shown in Equation 9.

$$\begin{bmatrix} n_2\theta_t \\ h_t \end{bmatrix} = \begin{bmatrix} 1 & -\mathcal{D} \\ 0 & 1 \end{bmatrix} \begin{bmatrix} n_1\theta_i \\ h_i \end{bmatrix} \tag{9}$$

The four-element matrix in Equation 9 is known as a refraction matrix ($\mathcal{R}$) and is defined generically as shown in Equation 10 [23].

$$\mathcal{R} = \begin{bmatrix} 1 & -\mathcal{D} \\ 0 & 1 \end{bmatrix} \tag{10}$$

Using $r_i = \begin{bmatrix} n_1\theta_i \\ h_i \end{bmatrix}$ and $r_t = \begin{bmatrix} n_2\theta_t \\ h_t \end{bmatrix}$ to represent the incident and reflected ray matrices respectively, Equation 9 can then be rewritten concisely as shown in Equation 11.

$$r_t = \mathcal{R} r_i \tag{11}$$

A ray traveling through a lens of thickness d can be similarly described when it is noted that the index of refraction is constant throughout the medium ($n_1 = n_2 = n$), there is no refraction within a single medium ($\theta_i = \theta_t$), and the relationship between h_i and h_t can be described using geometric relationships as shown in Equation 12. The resulting relationships are expressed in matrix form in Equation 13 [23].

$$h_i = d\theta_t + h_t \tag{12}$$

$$\begin{bmatrix} n_2\theta_t \\ h_t \end{bmatrix} = \begin{bmatrix} 1 & 0 \\ d/n & 1 \end{bmatrix} \begin{bmatrix} n_1\theta_i \\ h_i \end{bmatrix} \tag{13}$$

The four-element matrix in Equation 13 is known as a transfer matrix ($\mathcal{T}$) and is defined generically as shown in Equation 14 [23]. Equation 13 is similarly rewritten concisely as shown in Equation 15.

$$\mathcal{T} = \begin{bmatrix} 1 & 0 \\ d/n & 1 \end{bmatrix} \tag{14}$$

$$\mathcal{r}_t = \mathcal{T}\mathcal{r}_i \tag{15}$$

Refraction matrices and transfer matrices can be concatenated to describe a thick lens in the form of a system matrix ($\mathcal{A}$) [23]. As shown in Figure 13, an incident ray undergoes refraction at the first refracting surface (described by $\mathcal{R}_1$), travels a distance through the lens (described by $\mathcal{T}_{21}$), and undergoes refraction a second time at the second refracting surface (described by $\mathcal{A}_2$). The resulting system matrix is shown in Equation 16 and simplified as shown in Equation 17, with its relationship to the initial incident and final transmitted rays expressed concisely as shown in Equation 18.

$$\mathcal{A} = \mathcal{R}_2\mathcal{T}_{21}\mathcal{R}_1 = \begin{bmatrix} 1 & -\mathcal{D}_2 \\ 0 & 1 \end{bmatrix} \begin{bmatrix} 1 & 0 \\ d/n & 1 \end{bmatrix} \begin{bmatrix} 1 & -\mathcal{D}_1 \\ 0 & 1 \end{bmatrix} \tag{16}$$

$$\mathcal{A} = \begin{bmatrix} 1 - \frac{\mathcal{D}_2 d}{n} & -\mathcal{D}_1 - \mathcal{D}_2 + \frac{\mathcal{D}_1 \mathcal{D}_2 d}{n} \\ \frac{d}{n} & 1 - \frac{\mathcal{D}_1 d}{n} \end{bmatrix} \tag{17}$$

$$r_t = \mathcal{A} r_i \tag{18}$$

Using the system matrix, a thick lens can be modeled as a single refracting surface described by $\mathcal{A}$ rather than $\mathcal{R}$. Using Equation 10 to note that the negative of the dioptric power of a refracting surface is typically the top-right element of $\mathcal{R}$, the negative of the dioptric power of a thick lens can similarly be found by noting the top-right element of $\mathcal{A}$ as shown in Equation 19.

$$-\mathcal{D} = -\mathcal{D}_1 - \mathcal{D}_2 + \frac{\mathcal{D}_1 \mathcal{D}_2 d}{n} \tag{19}$$

Using Equation 7, Equation 19 can be rewritten as shown in Equation 20. The resulting equation is the lensmaker's equation, which defines the focal distance of any two-faced lens.

$$f = \left[(n-1) \left(\frac{1}{r_1} - \frac{1}{r_2} + \frac{(n-1)d}{r_1 r_2 n} \right) \right]^{-1} \tag{20}$$

Equation 20 is used to derive an expression for the focal length of a glass bead in Section 4.3, ultimately leading to a ray propagation model for retroreflections from aggregate roadway markings.

4.3. Ball Lenses

In terms of lens theory, spherical transmissive glass beads can be modeled as ball lenses, which are perfectly spherical as shown in Figure 14. The focal length (f_{ball}) is included in the figure, as well as points A, B, C, D, E, and F for reference purposes. Reflected and transmitted rays are shown at the interfaces formed at points B and C, with the majority of the energy originally associated with the incident ray ($\overline{AB}$) being associated with the transmitted rays ($\overline{BC}$ and $\overline{CD}$) rather than the reflected rays ($\overline{BE}$ and $\overline{CF}$). For a ball lens, the radii of curvature of both surfaces are equal ($r_1 = r_2 = r$) and the thickness of the lens is equal to the sum of the radii of curvature ($d = r_1 + r_2 = 2r$).

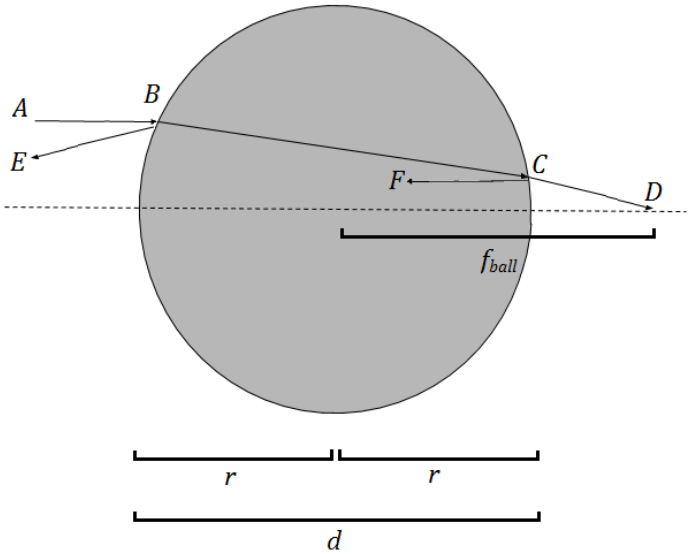

Figure 14: Ball lens cross-section diagram.

Using Equation 20 and the geometric relationships shown in Figure 14, the focal distance of a ball lens can be expressed as shown in Equation 21.

$$f_{ball} = \frac{nr}{2(n-1)} \tag{21}$$

The geometric path of any electromagnetic ray incident on a ball lens can thus be characterized by Equation 21, with the angles of reflected rays being characterized by Equation 4 and proportions of incident power associated with transmitted and reflected rays being characterized by Equation 5 and Equation 6 respectively. These relationships form the mathematical basis for all theoretical simulations included in this work (detailed in Section 7).

As an example, a diagram of a glass bead (ball lens) at 50% embedment in a highly reflective roadway marking binder is shown in Figure 15. The figure includes a ray ($\overline{AB}$) that is incident on the glass bead at an arbitrary polar angle (θ) at point B.

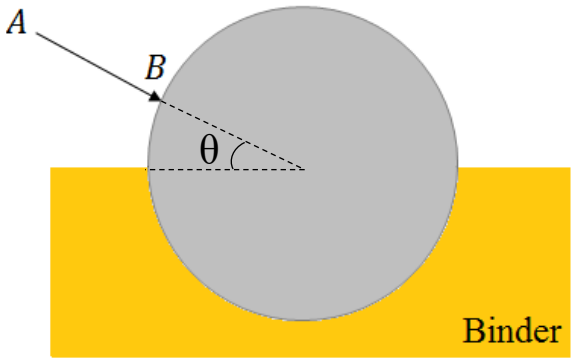

Figure 15: Diagram of glass bead (ball lens) embedded in binder.

Figure 15 is rotated so that the incident ray is horizontal as shown in Figure 16. The lensmaker's equation (Equation 21) is used to calculate the focal length, and the transmitted ray ($\overline{BC}$) from the interface at B propagates towards the end of the focal length. The low energy reflections described in Figure 14 are neglected in this example.

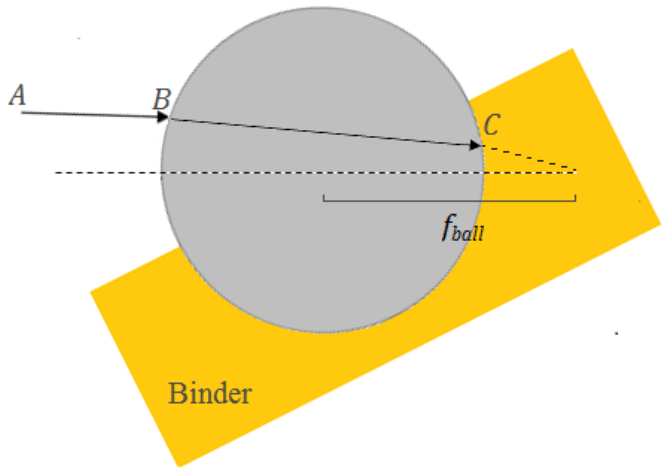

Figure 16: Diagram of glass bead (ball lens) embedded in binder with transmitted ray.

If the binder was not present in this example, the transmitted ray ($\overline{BC}$) from the interface at B would continue to propagate towards the end of the focal length. As this particular ray happens to become incident on a highly reflective bead-binder interface, however, a reflected ray ($\overline{CD}$) is formed at C according to the Law of Reflection (Equation 4) as shown in Figure 17. The propagation of this ray is once again determined by rotating the figure and applying the lensmaker's equation (Equation 21). Any additional interactions with the binder would also be similarly described by the Law of Reflection (Equation 4). The overall result of the particular interactions shown in Figure 17 is that a final ray ($\overline{DE}$) is formed such that it propagates in a direction approximately opposite to the direction of the initial incident ray ($\overline{AB}$). $\overline{DE}$ is therefore a retroreflection of $\overline{AB}$.

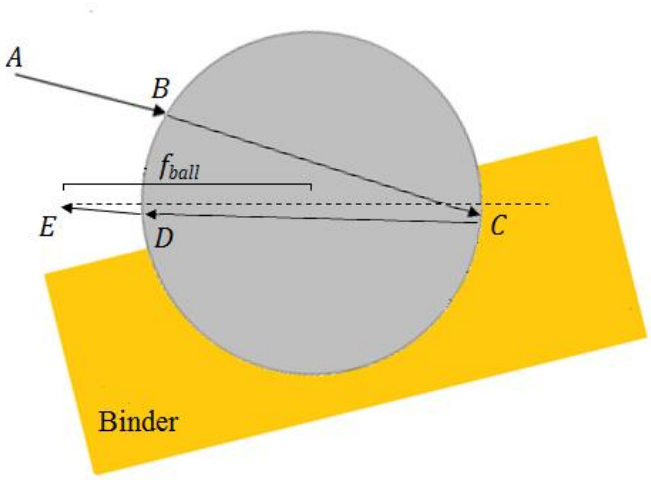

Figure 17: Diagram of glass bead (ball lens) embedded in binder with retroreflected ray.

This procedure is repeated for all possible incident polar angles in the simulations described in Section 7. The data produced by those simulations is calculated according to the relationships derived in this section, and is used to determine which polar angles produce retroreflections as detailed in Section 7.3.

The conditions required for glass beads embedded in roadway marking binders to produce retroreflections are therefore twofold: (1) The binder must be reflective for the particular electromagnetic radiation that is incident on the roadway marking; and (2) The initial incident electromagnetic ray must enter a glass bead in an orientation that allows the final transmitted electromagnetic ray to exit the bead in an orientation approximately opposite to that of the initial incident electromagnetic ray.

5. Azimuthal Angular Dependence Experiments

These experiments were performed in order to investigate the relationship between the azimuthal angle of observation and the retroreflective properties of roadway markings with and without embedded glass beads. A modified handheld retroreflectometer was used to take retroreflectivity measurements so that the light source and optical imager were set at fixed polar angles in accordance with standard 30-meter geometry (θ = 1.24° and θ = 2.29° respectively) [10]. The spherical coordinate system used in this work is defined as shown in Figure 11 in Section 3. The azimuthal angle was varied as shown in Figure 18.

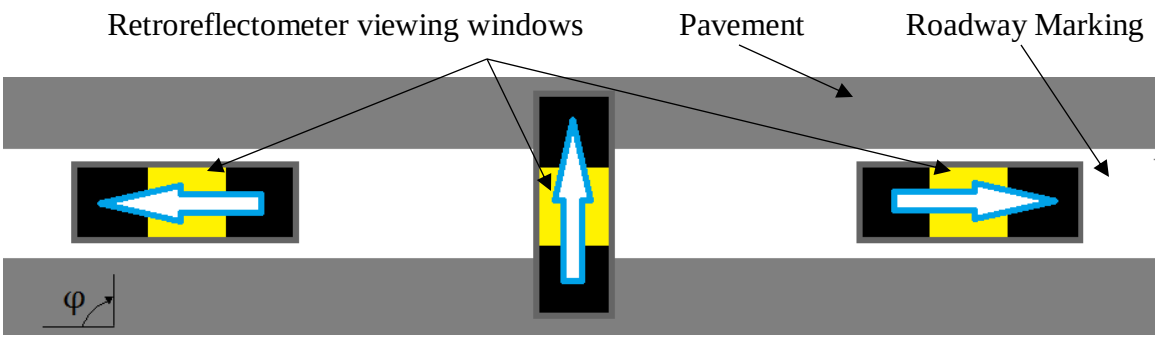

Figure 18: Retroreflectometer roadway marking measurement positions for azimuthal angles of 0° (left), 90° (center), and 180° (right).

5.1. Experimental Setup

Five white roadway marking samples with 6 inch (15.2 centimeter) widths were produced for the purposes of these experiments as described in Table 3. The binders for each sample were applied from standard roadway striping vehicles onto plywood boards so that the samples could be transported for testing purposes. As noted, Sample 3 and Sample 4 had glass beads applied by a bead gun mounted on the roadway striping vehicle while Sample 5 had its glass beads applied using a handcart application method so as to ensure that Sample 5 would not exhibit significant bead rolling effects. Special notation was made of the direction of application for each sample.

Table 3: Samples Applied for Azimuthal Angular Dependence Experiments

Sample	Binder	Bead Types
1	Paint	None
2	Epoxy	None
3	Paint	Type A
4	Epoxy	Type A + Type B
5	Epoxy	Type A + Type B (handcart applied)

Type A and Type B glass beads were manufactured according to specifications prescribed by PennDOT. Mounted bead gun and handcart applicators are shown in Figure 19.

Figure 19: Bead gun applicator (left) and bead handcart applicator (right).

Each sample was subjected to three sets of 20 retroreflectivity measurements, yielding 60 total measurements for each sample. The first set was taken in the direction of application (azimuthal angle denoted as 0°), the second in a direction orthogonal to the direction of application (azimuthal angle denoted as 90°), and the third in the direction directly opposite to the direction of application (azimuthal angle denoted as 180°). Each of the three data sets were then compared to each other and statistically analyzed using a standard T-test in order to determine if the sample had a statistically significant dependence between retroreflectivity and direction of observation.

5.2. Measurement Instrumentation

All retroreflectivity measurements were taken with a modified Delta LTL-X handheld retroreflectometer (shown in Figure 20). Using 30-meter geometry, the device directs a broad spectrum white light source towards the material in the specified viewing window and measures the luminous intensity of the light that is reflected back towards

the light receiver. The coefficient of retroreflected luminance can then be calculated as the ratio of the reflected luminance of the light to the overall illuminance normal to the viewing window.

Figure 20: Modified Delta LTL-X handheld retroreflectometer.

The Delta LTL-X includes a viewing window with dimensions of 2 inches by 8 inches (5.1 centimeters by 20.3 centimeters). This is an unacceptably large area when taking retroreflectivity measurements of roadway lines measuring 4 inches (10.2 centimeters) or 6 inches (15.2 centimeters) laterally across from orthogonal directions (denoted as 90°). All samples in these experiments were produced to measure 6 inches (15.2 centimeters) laterally across, which is not long enough to sufficiently fill the viewing window of the Delta LTL-X. Raw measurements taken in this fashion would be

inaccurate, as fractions of the incident light would reflect off materials that were not intended to be included in the sample measurements.

To overcome this challenge, the Delta LTL-X viewing window was reduced to accommodate orthogonal measurements of 6 inch (15.2 centimeter) wide roadway markings. A boot manufactured from black tar paper was fastened to the bottom of the device as shown in Figure 21 (adapted from [11]). Preliminary measurements indicated that the 30-meter geometry retroreflectivity of the tar paper was negligibly low (between 3 to 4 millicandelas per square meter per lux), indicating that the boot would not artificially influence retroreflectivity measurements. The boot included a small viewing window with dimensions of 2 inches by 3 inches (5.1 centimeters by 7.6 centimeters) so that material samples within that window could still be measured and tested. This methodology ensured that consistent retroreflectivity measurements could be taken at every azimuthal angle.

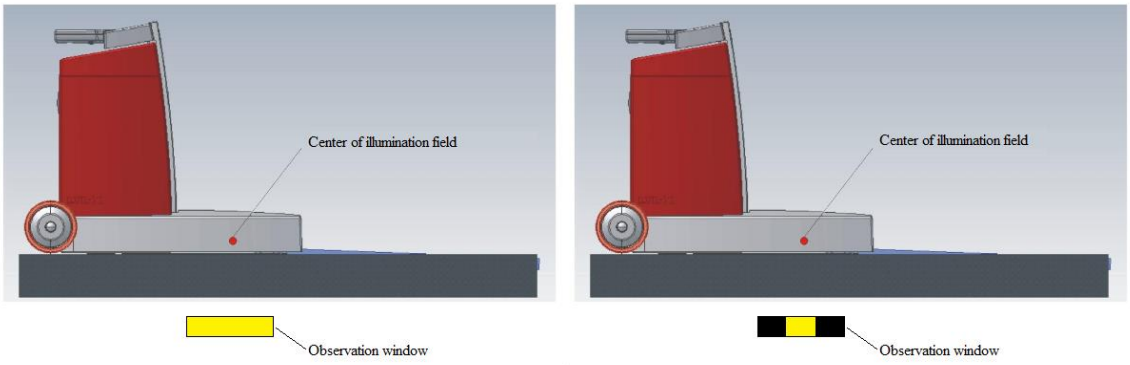

Figure 21: Delta LTL-X observation window without boot (left) and with boot (right).

The boot modification effectively reduced the area of the viewing window by a factor of 16:6. This artificially lowered the raw measurements as the calculations performed by the Delta LTL-X assume a larger viewing window than was actually in use. To compensate for this, all retroreflectivity measurements were scaled by the specified 16:6 scaling factor in order to produce a value that would correspond to the actual retroreflectivity of the sample. The validity of this methodology was confirmed by a series of measurements with and without the boot modification at an azimuthal angle of 0°. Measured values taken with the reduced viewing window were scaled by the specified scaling factor and found to be consistent with the measurements taken without the reduced viewing window.

5.3. Results and Analysis

Experimental results are summarized in box diagrams as shown in Figure 22, Figure 23, Figure 24, Figure 25, and Figure 26. All data sets were acquired using the described methodology and scaled by the appropriate scaling factor in order to account for the size of the modified viewing window of the retroreflectometer. Raw measurements are included in Appendix B.

Table 4, Table 5, and Table 6 include summaries of the test data for each of the five samples. The sampled distributions measured at azimuthal angles of 90° and 180° were compared to the sampled distributions measured at an azimuthal angle of 0° for each sample. An α value of 0.05 was chosen to account for the natural variance that can

occur when performing retroreflectivity measurements. A rejection of the null hypothesis would indicate that there is a statistical difference between the means of each sampled distribution (with 95% confidence), suggesting that the retroreflectivity of the sample varies with respect to the azimuthal angle of observation for the measured geometry.

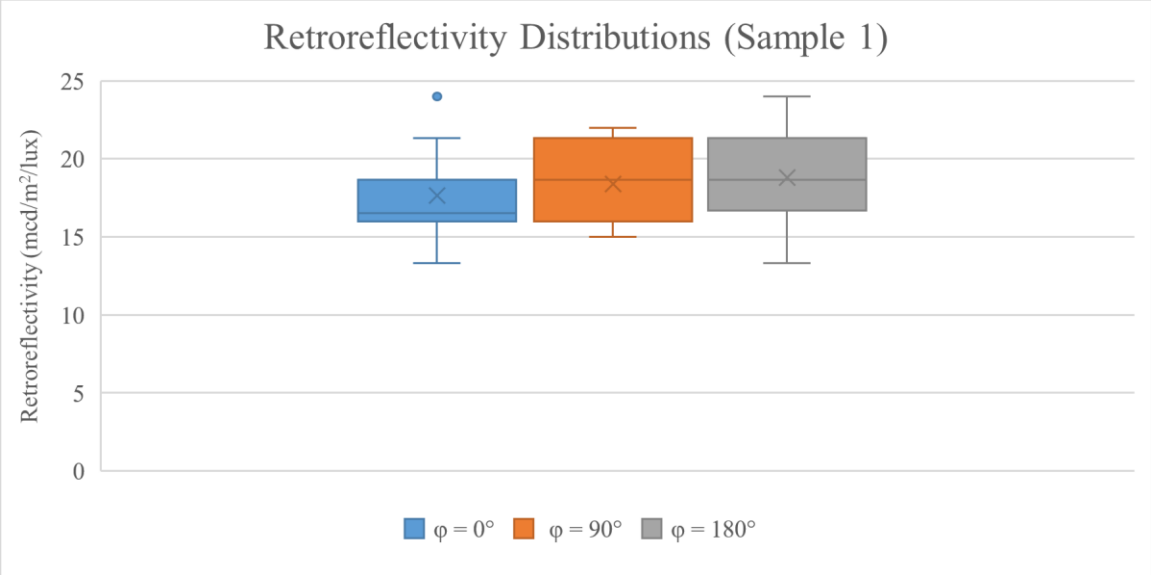

Figure 22: Azimuthal angular dependence measured retroreflectivity distributions (Sample 1).

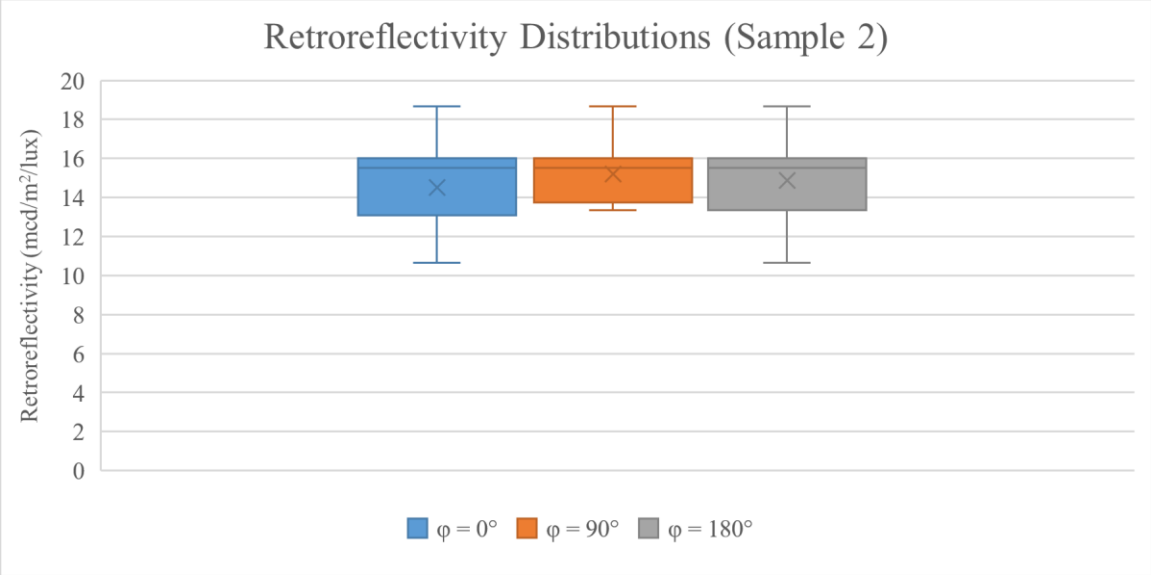

Figure 23: Azimuthal angular dependence measured retroreflectivity distributions (Sample 2).

Table 4: Azimuthal Angular Dependence T-Test Results (Samples 1-2)

	Sample 1		**Sample 2**	
Binder	Paint		Epoxy	
Bead Applicator	Bead Gun		Bead Gun	
Bead Type(s)	None		None	
Measurement Direction	90°	180°	90°	180°
α Value	0.05	0.05	0.05	0.05
T-Test Result	0.383	0.221	0.304	1.000
Null Hypothesis Rejection	no	no	no	no

Sample 1 (Figure 22) and Sample 2 (Figure 23) did not have any glass beads or reflective material deposited onto them so that the only material being measured would be the paint and epoxy binders. These tests were performed in order to establish a measurement baseline and confirm that there were no azimuthal angular reflectivity relationships associated with the binders themselves. Test results showed a high level of

consistency between the measured values at each angle, suggesting that there is indeed no azimuthal angular relationship associated with the binders for the measured geometry.

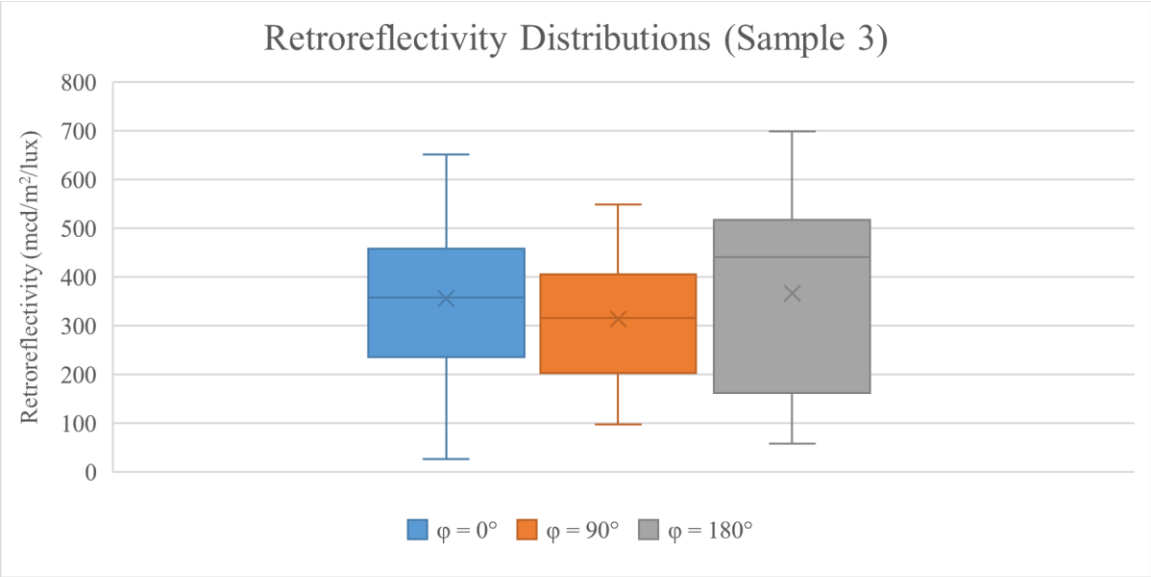

Figure 24: Azimuthal angular dependence measured retroreflectivity distributions (Sample 3).

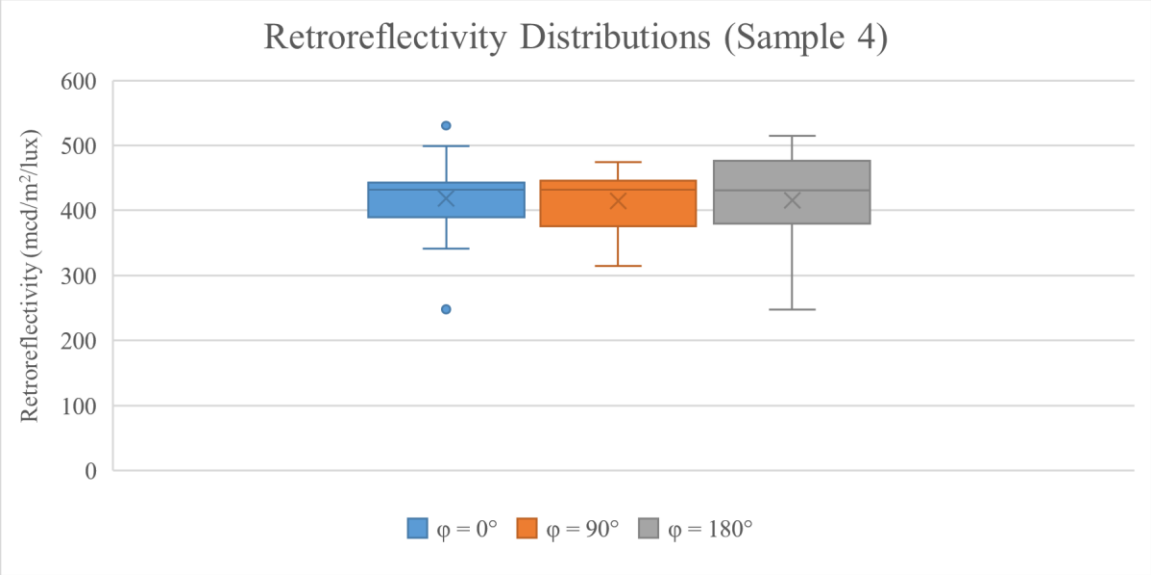

Figure 25: Azimuthal angular dependence measured retroreflectivity distributions (Sample 4).

Table 5: Azimuthal Angular Dependence T-Test Results (Samples 3-4)

	Sample 3		**Sample 4**	
Binder	Paint		Epoxy	
Bead Applicator	Bead Gun		Bead Gun	
Bead Type(s)	Type A		Type A + Type B	
Measurement Direction	90°	180°	90°	180°
α Value	0.05	0.05	0.05	0.05
T-Test Result	0.401	0.876	0.824	0.911
Null Hypothesis Rejection	no	no	no	no

Sample 3 (Figure 24) and Sample 4 (Figure 25) were more typical samples, applied using the same methodology that would typically be used when applying roadway markings from a roadway striping vehicle. Type A beads were deposited onto the paint sample (Sample 3) and both Type A and Type B beads were deposited onto the epoxy sample (Sample 4). Both samples showed consistency between the measurements

at each azimuthal angle, indicating that there is no azimuthal angular relationship associated with the glass beads used in this study for the measured geometry when the glass beads are correctly applied using a zero-velocity bead drop methodology.

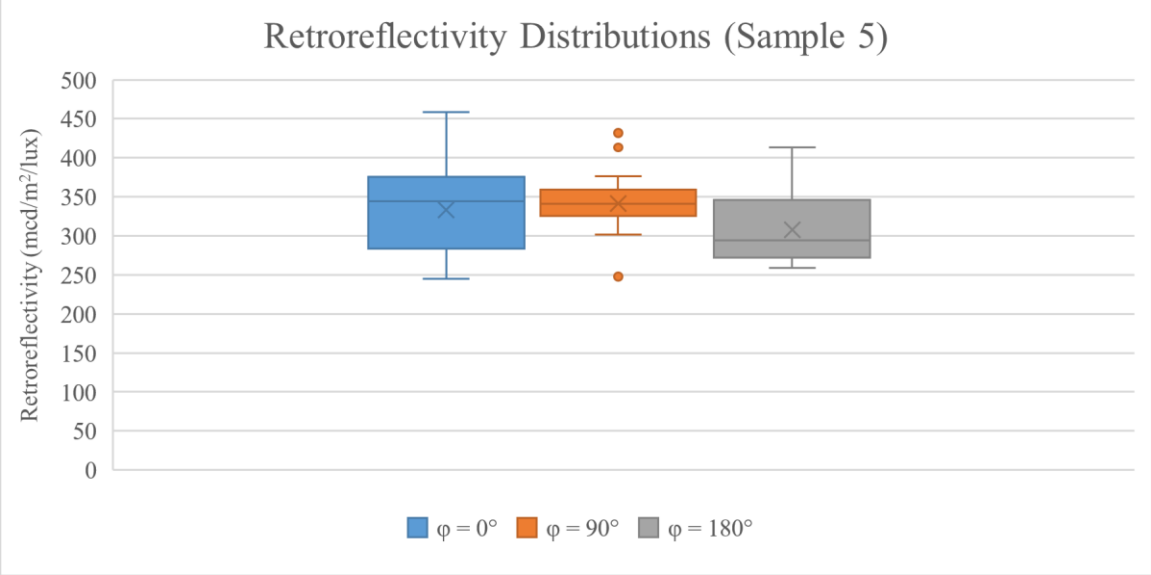

Figure 26: Azimuthal angular dependence measured retroreflectivity distributions (Sample 5).

Table 6: Azimuthal Angular Dependence T-Test Results (Sample 5)

	Sample 5	
Binder	Epoxy	
Bead Applicator	Handcart Applicator	
Bead Type(s)	Type A + Type B	
Measurement Direction	90°	180°
α Value	0.05	0.05
T-Test Result	0.420	0.142
Null Hypothesis Rejection	no	no

Sample 5 (Figure 26) was similar to Sample 4, except that the beads were applied using a handcart applicator rather than the bead gun. As handcart bead application must be performed at a much slower velocity, this application method should have ensured that Sample 5 would not exhibit any significant bead rolling effects. The sample was therefore used as a control for this set of experiments, indicating that the measurements taken on Sample 3 and Sample 4 are consistent with that of a sample with completely symmetric bead embedment.

It is important to note that the validity of all of these results is limited to machine vision system configurations where the light source and optical imager are fixed at polar angles of 1.24° and 2.29° respectively. However, the lack of a statistically significant relationship between the azimuthal angle of observation and the measured reflectivity coupled with an understanding of the optical symmetry of ball lenses (as described in Section 4.3) strongly indicates that there is similarly no azimuthal angular relationship when a light source and optical imager are placed at any set of polar angles. This assumption (based on measured data) is used as part of the theoretical basis for the optical model described in Section 7.

6. Binder Reflectivity Experiments

These experiments were performed in order to investigate the relationship between the reflective properties of roadway marking binders (without glass beads) and the electromagnetic wavelengths that may be incident on them in a machine vision system. A light source (high power, multi-color light emitting diodes (LEDs)) and an optical imager (digital illuminance meter) were fixed at equivalent polar angles (θ) within a plane of incidence that included a target (roadway marking binder sample) as shown in Figure 27.

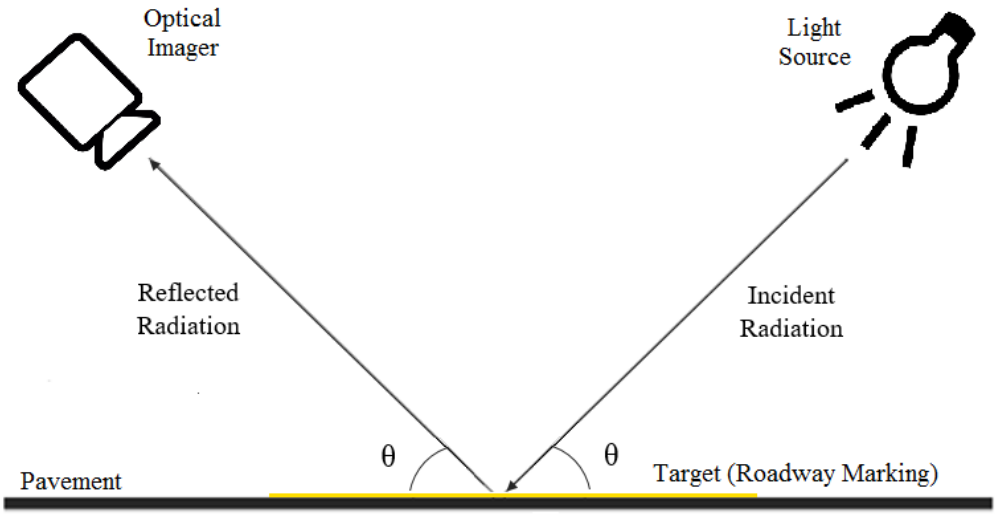

Figure 27: Machine vision equivalent polar angles positional diagram.

For three different targets (a white roadway marking binder sample, a yellow roadway marking binder sample, and a mirror), the wavelengths emitted from the light source were varied between four spectrums corresponding to red, green, blue, and violet visible light. The resulting reflected illuminance was measured by the optical imager, and the process was performed at symmetric polar angles of 30°, 50°, and 70° for each target. Illuminance measurements associated with the roadway marking targets are compared to the illuminance measurements associated with the mirror target (which is assumed to act as a perfect reflector) in order to account for the spectral responsivity of the digital illuminance meter and measure approximate spectral reflectivity responses for the roadway marking binders.

6.1. Experimental Setup

Two roadway marking epoxy binder samples were used as targets in these experiments. Both samples were applied from a standard roadway striping vehicle onto plywood boards so that the samples could be transported for testing purposes. No beads were dispensed onto these samples, as the purpose of these experiments was to investigate the reflective properties of only the roadway marking binders. Black tar paper was used to cover all portions of the plywood boards not covered by the applied binder as shown in Figure 28, as the tar paper can be expected not to reflect significant amounts of

electromagnetic radiation in the visible spectrum. The boards were covered such that the exposed surface areas of both binder samples were approximately equivalent.

Figure 28: White (left) and yellow (right) roadway marking binder samples (without glass beads).

A LED Engin LuxiGen LZ7-04MU00 multi-color LED package was used as a light source in these experiments. The package is shown in Figure 29, with information pertaining to the optical characteristics of the LEDs in the package included in Table 7 [25]. Individual LEDs were powered during the experiments such that only one colored LED was active at a time.

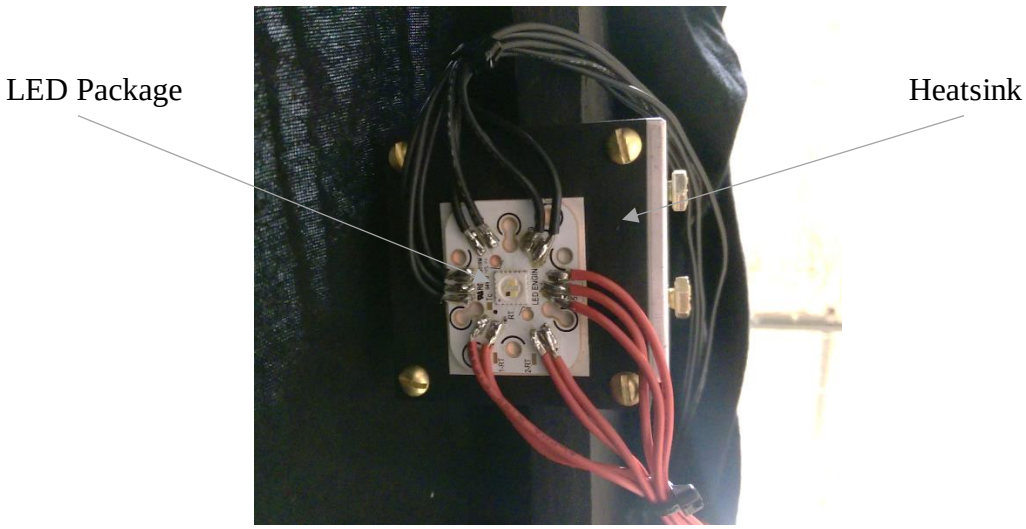

Figure 29: LED Engin LuxiGen LZ7-04MU00 package mounted on a heatsink.

Table 7: LED Engin LuxiGen LZ7-04MU00 Package Optical Characteristics

LED Color	Maximum Luminous Flux (lm)	Dominant Wavelength (nm)
Red	105	623
Green	166	523
Blue	35	457
Violet	66	395

A plywood arc was constructed for the purpose of securing the light source and optical imager at equivalent polar angles with respect to the target as shown in Figure 30. The arc was constructed such that the light source and optical imager could be mounted along a plane at polar angles ranging from 0° to 180° with a fixed radial distance of 1.0 meter. A separating barrier was included in the midsection of the arc so that radiation emitted from the light source could not reach the optical imager without first being reflected from the target. The entire arc structure was also covered with a black opaque cloth in order to more fully ensure that the only involved surface capable of reflecting

significant amounts of electromagnetic radiation within the visible spectrum would be the target.

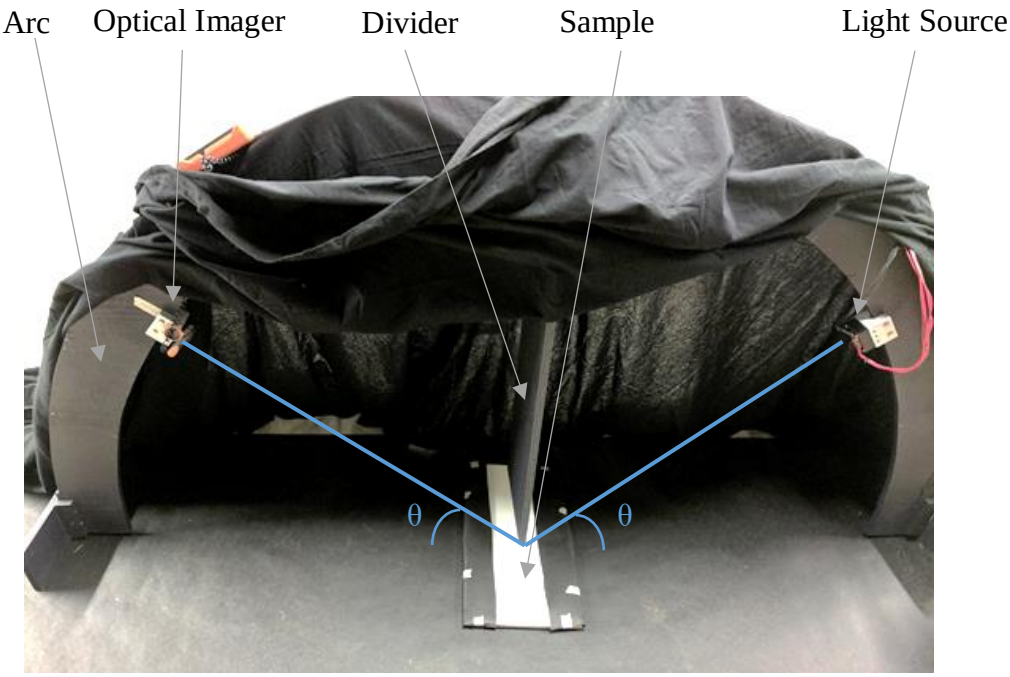

Figure 30: Plywood arc with mounted digital illuminance meter and light source.

6.2. Measurement Instrumentation

A Dr. Meter LX1330B digital illuminance meter was used as an optical imager in these experiments. The meter receptor was mounted on the arc at an equivalent polar angle to the light source as shown in Figure 31 with the meter display made visible on the outside of the arc. All visible spectrum electromagnetic radition incident on the receptor is weighted by the device's spectral responsivity to produce an illuminance measurement.

Figure 31: Dr. Meter LX1330B digital illuminance meter receptor (left) and display (right).

As previously described, the three targets included in these experiments were a white roadway marking binder sample (without glass beads), a yellow roadway marking binder sample (without glass beads), and a mirror. For optical frequencies, a flat mirror may approximately behave as an ideal reflector (where $R \approx 1$). Due to this behavior, when the mirror was used as a target, the illuminance measured by the optical imager was approximately equal to the illuminance of the radiation incident on a certain sectional area of the target (weighted by the meter's spectral responsivity).

Reflectivity values are therefore calculated as the ratios of illuminance values measured for binder targets to illuminance values measured for the mirror target for constant incident wavelengths, incident light intensities, and machine vision system geometric configurations. As the spectral responsivity weighting was constant for all measured illuminance values, the described ratio reduces to a ratio of incident radiant fluxes, ultimately yielding a value for the reflectivity of the binder material.

6.3. Results and Analysis

Experimental results are summarized in scatter plots as shown in Figure 32 and Figure 33. All data sets were acquired using the described methodology, with the reflectivity values being the described ratios of illuminance measurements for the binder targets to illuminance measurements for the mirror target. Raw measurements are included in Appendix C.

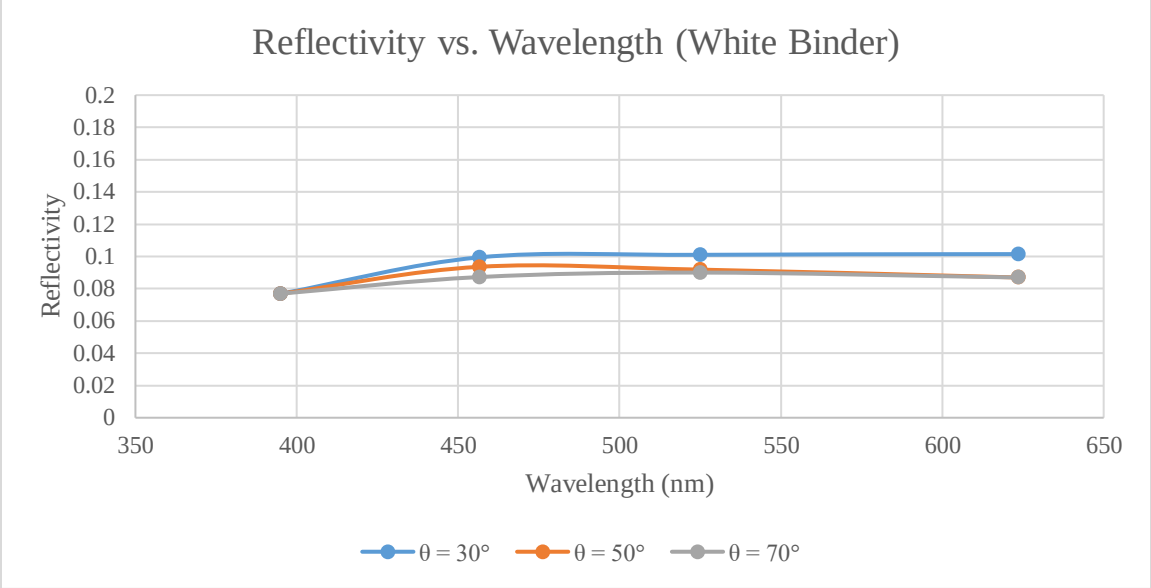

Figure 32: Binder reflectivity measured wavelength relationship (white binder).

The white roadway marking binder sample (Figure 32) exhibited consistent reflectivity values across the visible spectrum in these experiments, except for dominant incident wavelengths of 395 nanometers. A small decrease in reflectivity (between 1% to

2%) was observed at this wavelength, possibly indicating a decreasing reflectivity trend for incident wavelengths in the ultraviolet spectrum. These results are otherwise consistent with what may be expected from the observed color of the sample, as a white color typically indicates that the reflected radiation contains wavelengths spanning the entirety of the visible spectrum. No significant changes in reflectivity were observed when the polar angles of the light source and imager were varied.

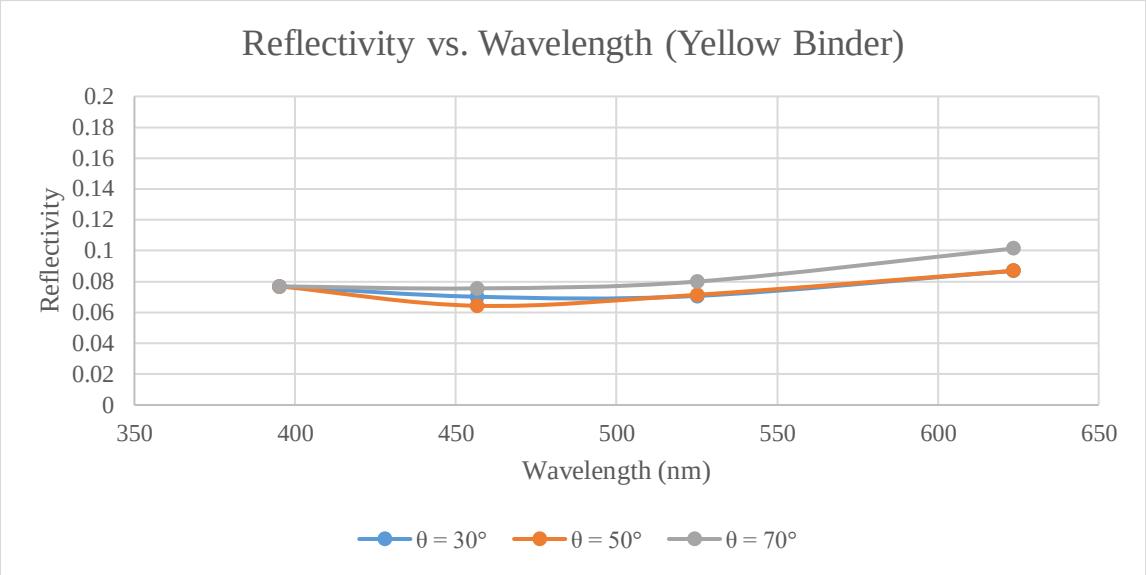

Figure 33: Binder reflectivity measured wavelength relationship (yellow binder).

The yellow roadway marking binder sample (Figure 33) exhibited its highest reflectivity values for dominant incident wavelengths of 623 nanometers. The sample exhibited reflectivity values that were between 2% to 3% lower for other incident wavelengths, with the lowest reflectivity values being measured for dominant incident wavelengths of 457 nanometers. These results are consistent with what may be expected

from the observed color of the sample, as a yellow color typically indicates that the reflected radiation should predominantly contain larger wavelengths within the visible spectrum. No significant changes in reflectivity were observed when the polar angles of the light source and imager were varied.

Both roadway marking binder samples exhibited similar reflectivity values for the larger wavelengths in the visible spectrum (both samples specifically exhibited similar reflectivity values for dominant incident wavelengths of 623 nanometers). As the yellow roadway marking binder sample exhibited lower reflectivity values for other dominant incident wavelengths, the results of this experiment suggest that light sources which emit light containing larger wavelengths of visible light (corresponding to red, orange, or yellow light) may produce larger reflected signal intensities than light sources which do not emit light containing those wavelengths.

It is important to note that the described experimental setup did not account for the influence of scattering effects. If the roadway marking binder samples induced a significant amount of scattering in the reflected electromagnetic waves, then a certain amount of error may have been introduced into the measured reflectivity values. However, the consistency of the distributions of the measured values with the results that may be expected given the observed colors of the samples indicates that these results may still have some validity. Specifically, these experiments certainly provide a strong indication that roadway marking binders may be expected to exhibit at least some reflectivity throughout the visible spectrum. This assumption (based on measured data) is used as part of the theoretical basis for the optical model described in Section 7.

7. Optical Model Simulations

These simulations were performed in order to investigate the theoretical relationship between the reflective properties of roadway marking targets and the respective polar angles of the light source and optical imager components of a machine vision system. An optical model was designed in accordance with the experimental findings detailed in Section 5.3 and Section 6.3 and was constructed within an optical engineering software package for the purpose of efficient simulation. The polar angles of a simulated light source and optical imager (θ_1 and θ_2 respectively) were varied within a plane of incidence as shown in Figure 34 for roadway marking targets with various bead embedment levels. Using a geometrical optical model, ideal planar positions for the optical imager were calculated for each simulated light source position in order to maximize the received electromagnetic energy, thereby also maximizing the reflected signal intensity.

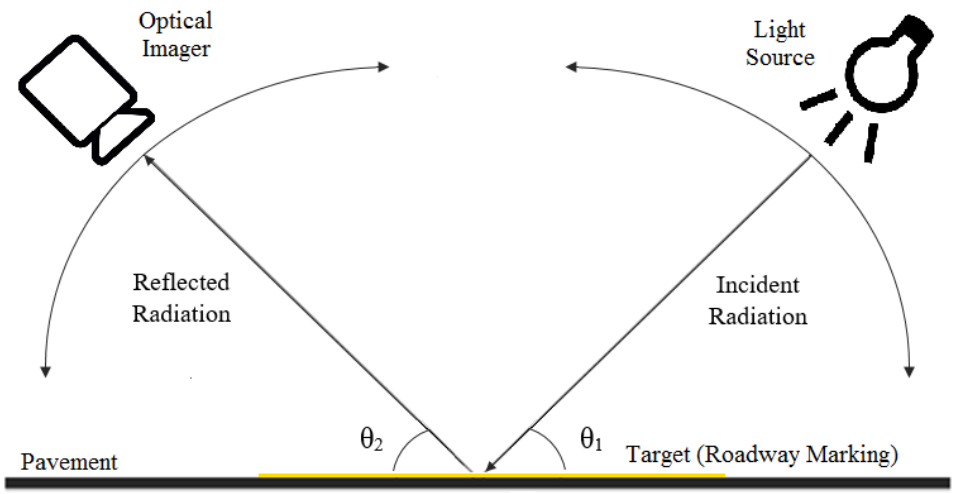

Figure 34: Machine vision independent polar angles positional diagram.

Glass bead embedment levels were varied as shown in Figure 35. A bead embedment level of 100% indicates that a bead is entirely below the surface of the roadway marking binder, while a bead embedment level of 0% indicates that a bead is entirely above the surface of the roadway marking binder. As discussed in Section 2.3, bead application rates are typically set such that a majority of the beads become embedded in the binder at an embedment level of 50%. However, other bead embedment levels were included in the simulations in order to gain a fuller understanding of the optical mechanisms that result in the observed electromagnetic properties of composite roadway markings.

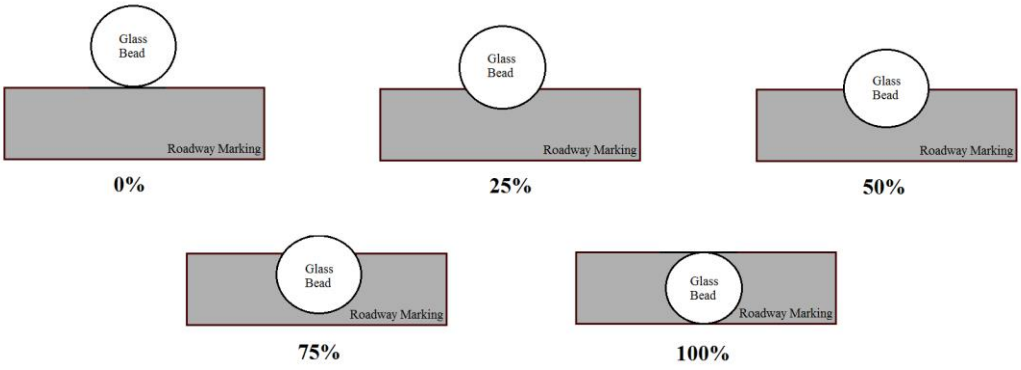

Figure 35: Optical model simulations glass bead embedment levels.

7.1. Model Details

The optical model was constructed using Photon Engineering FRED Optical Engineering Software, a raytracing software program capable of simulating the propagation of light through any optomechanical system. Glass beads were modeled as perfectly spherical permeable lenses with refractive indices of 1.5, while the roadway marking binder was modeled as an ideally reflective surface. Five glass beads were included in the model, each with a different embedment level as shown in Figure 35. The final resulting model included multiple bead-binder interfaces as shown in Figure 36, with the roadway marking binder material shown in yellow and the glass beads shown in gray. Additional modifications could be made to this model to account for changes in glass bead or binder parameters.

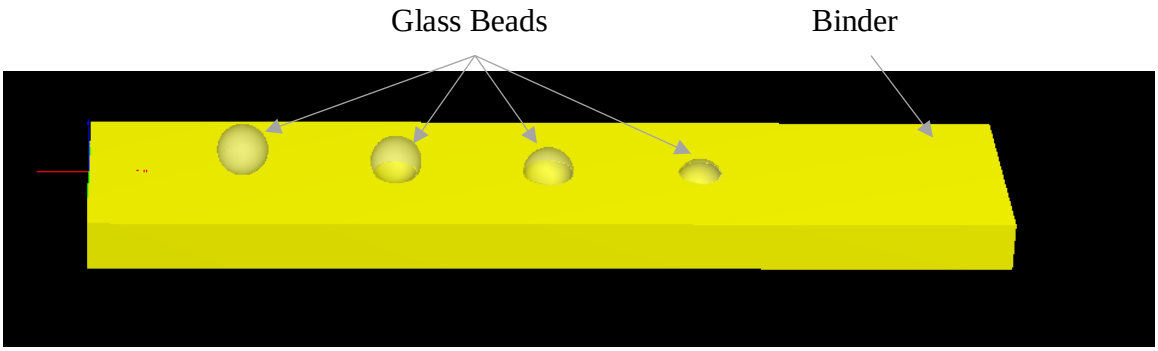

Figure 36: Optical model for multiple bead-binder interfaces.

A real-world roadway marking will of course contain a much larger number of embedded glass beads than were included in this model, depending on the type of binder used and the types of beads applied to it. The effective optical properties of aggregate roadway marking material, however, can be modeled as a superposition of the many interactions between incident radiation and each individual bead-binder interface. Simulation results obtained when using the model shown in Figure 36 can therefore still be used to predict the behavior of aggregate roadway marking material when the majority of the glass beads embedded in the material conform to the embedment levels included in the model.

The glass beads were modeled as perfectly spherical ball lenses, with no defects or other variations that would change with respect to the azimuthal angle of observation. The bead-binder interfaces formed where the glass beads are adjacent to the binder material were also modeled so that they would not change with respect to the azimuthal angle of observation. This portion of the model was designed in accordance with the findings detailed in Section 5.3, which indicate that the optical characteristics of typical

roadway markings may not be expected to change with respect to the azimuthal angle of observation.

The binder material was modeled as an ideally reflective surface with no material scattering effects for all incident electromagnetic wavelengths. Absorption effects are assumed to be negligible, and all reflected rays behave as described by the Law of Reflection. This portion of the model was designed in accordance with the findings detailed in Section 6.3, which indicate that a typical roadway marking binder may be expected to exhibit reflection effects across all electromagnetic wavelengths within the visible spectrum whether the binder is white or yellow.

7.2. Simulation Setup

Two types of light sources were used in these simulations; point light sources and plane light sources. For the purposes of this simulation, the point light sources produced simulated single light rays that behaved according to a geometric optical model. The point light sources were placed at polar angles varying from $\theta = 1°$ to $\theta = 90°$ at 1° intervals relative to each of the five glass beads as shown in Figure 37, which each white point in the figure representing one of the point light sources. A total of 90 light sources were placed relative to each glass bead.

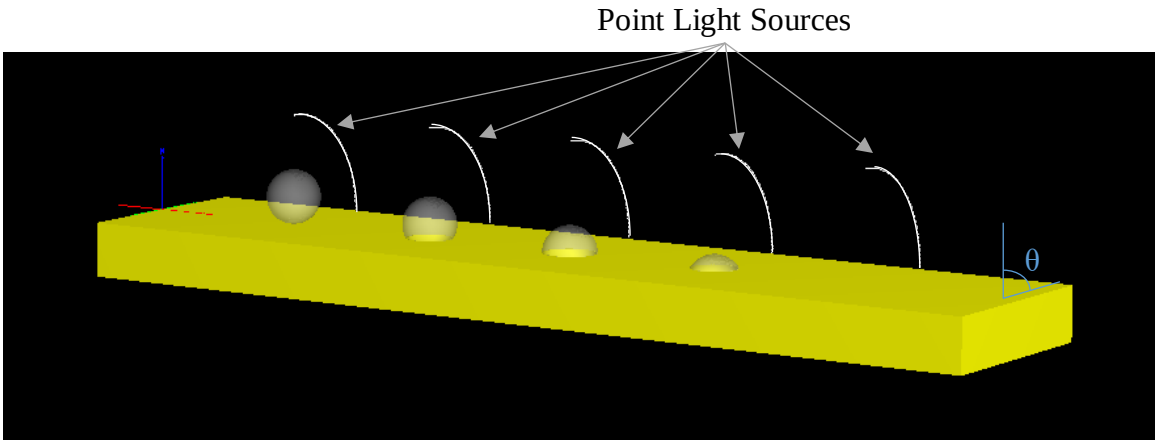

Figure 37: Optical model with point light sources (θ = 0° to θ = 90°).

For the purposes of the simulation, the plane light sources produced simulated plane waves that were a superposition of multiple single rays, with each plane wave being composed of an 11 x 11 array of individual single rays positioned within a single plane. Each plane with was therefore composed of 121 individual single rays. A total of 90 plane waves were placed at polar angles varying from θ = 1° to θ = 90° at 1° intervals relative to each of the five glass beads as shown in Figure 38. In this case, a plane wave is defined to be incident at a specified polar angle (θ) when the vector normal to center of the plane wave forms an angle θ with the surface of the roadway marking binder.

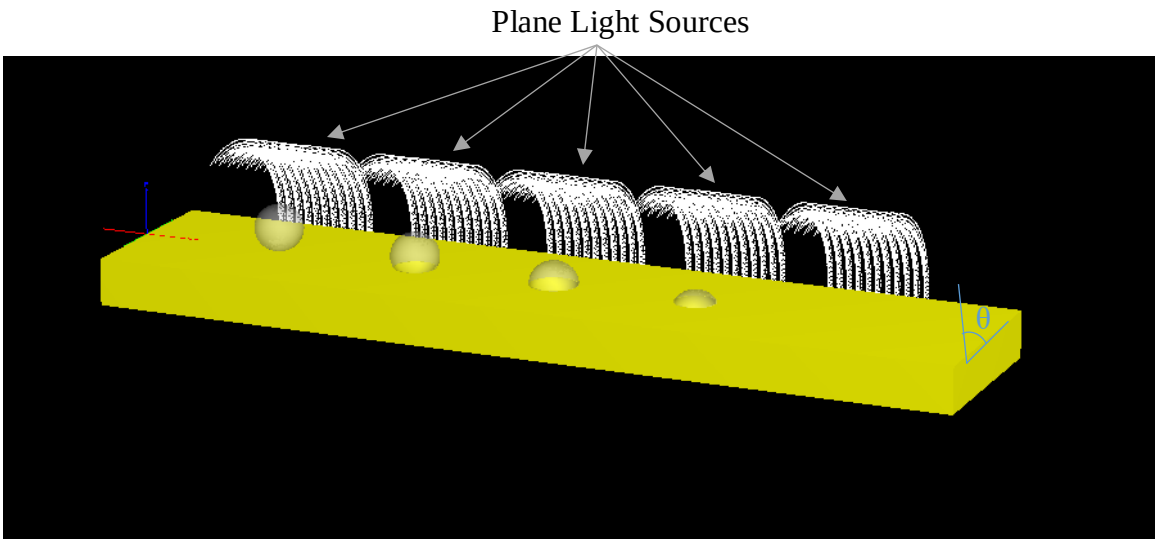

Figure 38: Optical model with plane light sources (θ = 0° to θ = 90°).

Two example plane light sources are shown in Figure 39, with the plane light source incident on the left bead being placed at a polar angle of 40° and the plane light source incident on the right bead being placed at a polar angle of 80°. The light sources are shown with and without their associated rays for further illustration. In the top image, a white line is draft from the glass beads to the centers of the plane light sources such that each line is normal to each light source. The angle that this line forms with the binder is the polar angle of the plane light source. In the bottom image, the 121 rays associated with each light source are shown propagating and interacting with the roadway marking model. The light source positioned at θ = 40° relative to its associated glass bead results in only some retroreflected rays, while the light source positioned at θ = 80° relative to its associated glass bead at shows significantly more retroreflections.

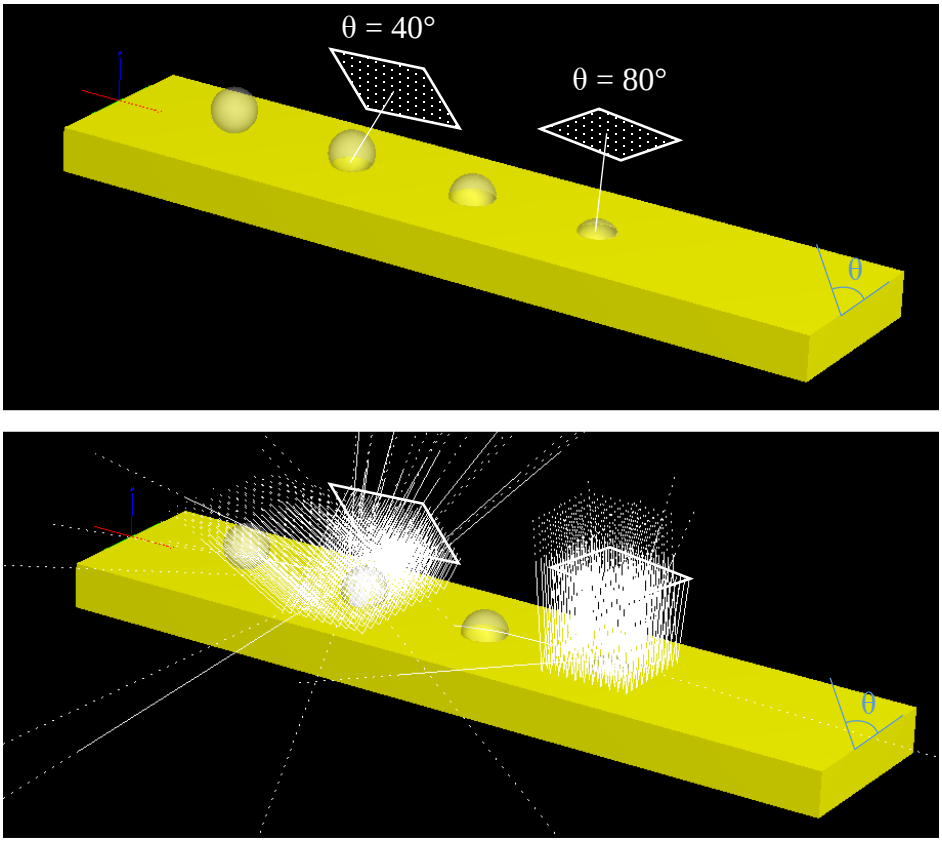

Figure 39: Example plane (121 ray) light sources (top) with associated light rays (bottom).

Each individual single ray was simulated using the Photon Engineering FRED Optical Engineering Software. The simulated rays were made to propagate in accordance with the geometric optical model. During the simulation, each individual single ray propagated towards the roadway marking model, underwent a series of reflections and refractions according to the geometry of the roadway marking model, and finally propagated away from roadway marking model as shown in Figure 40. For the point light sources, the final reflected polar angle was recorded along with its associated incident polar angle. For the plane light sources, the final reflected polar angles of every

individual single ray component of each plane wave was recorded along with their associated incident polar angles.

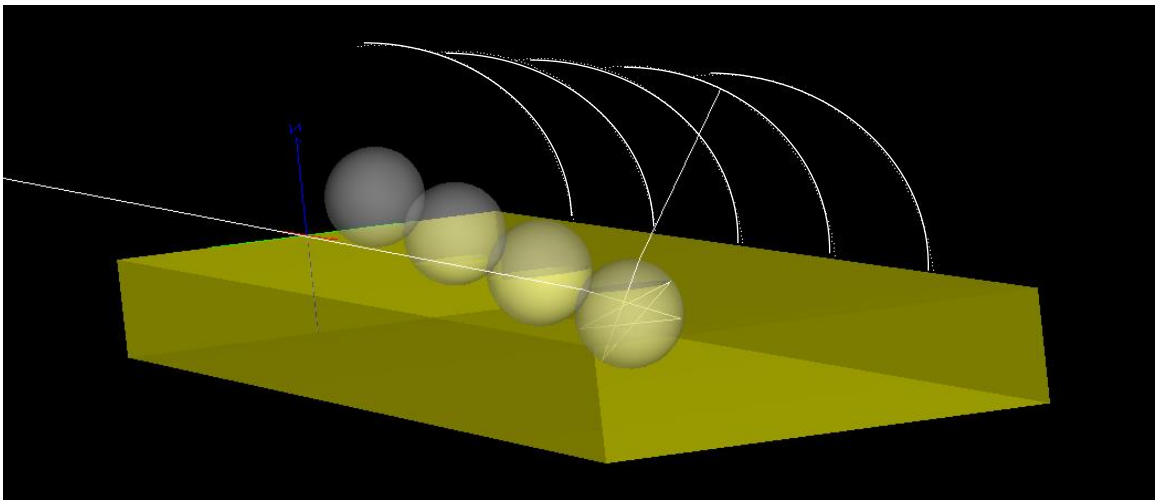

Figure 40: Example simulated bead-binder incident light interaction.

7.3. Results and Analysis

Point light source simulation results for the aggregate roadway marking model are summarized in a scatter plot as shown in Figure 41. All data sets were generated using the described methodology for point light sources, with the incident and reflected polar angles being defined with respect to the surface of the simulated roadway marking. Low-energy ray reflections and transmissions are neglected in the figure so that only the relationships between the initial high-energy incident rays and final high-energy transmitted rays of the aggregate roadway marking model are shown. Data points

corresponding to geometric configurations which produced significant amounts of reflected rays with polar angles of less than 90° are circled for additional emphasis.

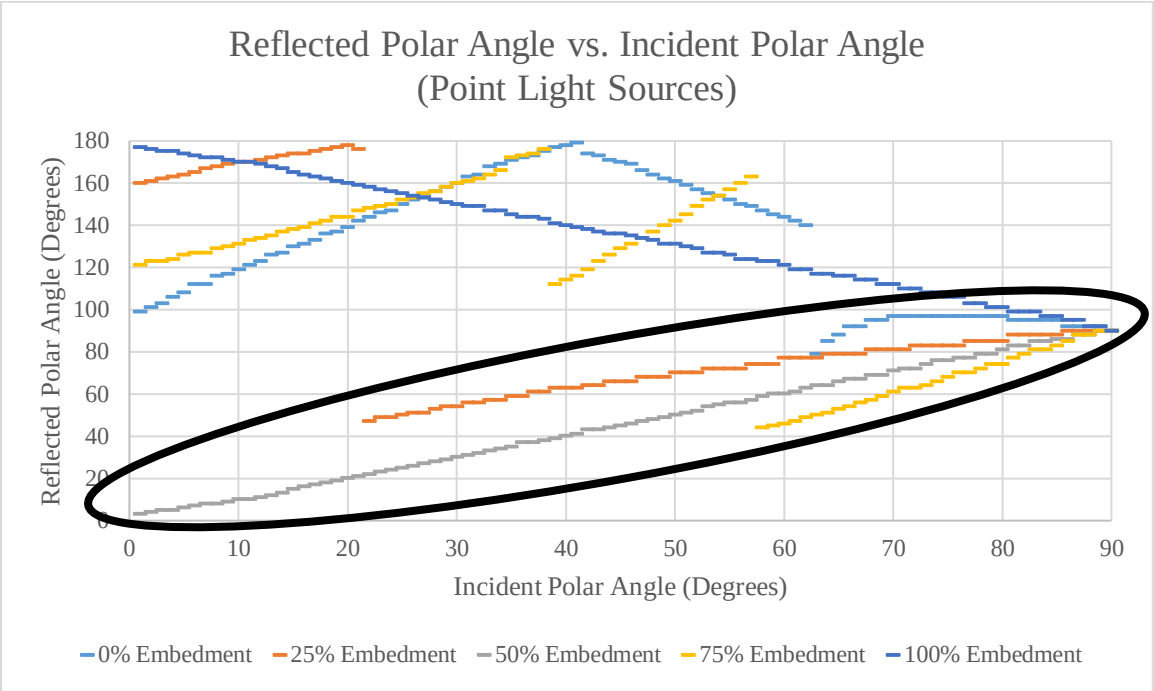

Figure 41: Optical simulations point light source angle relationships.

The point light source simulations (Figure 41) produced significant amounts of reflected rays with polar angles of less than 90° for glass bead embedments of 25%, 50%, and 75%. These reflections occurred for incident polar angles between 22° and 90° at 25% embedment, between 0° and 90° at 50% embedment, and between 58° and 90° at 75% embedment. Additional reflected rays were observed at polar angles greater than 90° for all embedment levels other than 50%. The reflections associated with glass beads at 50% embedment are true retroreflections, as the reflected rays propagated in the direction

exactly opposite to the direction of incident ray propagation in that case. For glass beads at 100% embedment (where only the binder interacted with the incident rays), the material behaved as described by the Law of Reflection.

It is relevant to note that reflected rays with polar angles of 90° were observed for incident rays with polar angles of 90° for all embedment levels. This result suggests that the signal intensity received by a machine vision system imaging roadway markings may be maximized when the light source and optical imager are both positioned at polar angles of 90° relative to the target. Additionally, given the prevalence of glass beads at 50% embedment in roadway markings (and to a lesser extent, the prevalence of glass beads at 25% and 75% embedments), these results also suggest that significant signal intensities may be measured whenever the polar angles of the light source and optical imager are equal.

Plane light source simulation results for the aggregate roadway marking model are summarized in scatter plots as shown in Figure 42, Figure 43, Figure 44, Figure 45, and Figure 46. All data sets were generated using the described methodology for plane light sources, with the incident and reflected polar angles being defined with respect to the surface of the simulated roadway marking. Low-energy ray reflections and transmissions are neglected in the figure so that only the relationships between the initial high-energy incident rays and final high-energy transmitted rays of the aggregate roadway marking model are shown. Portions of each plane light source were incident on various parts of the glass bead or binder portions of the roadway marking model, resulting in distributions of reflected polar angles being related to each incident polar

angle. Data points corresponding to geometric configurations which produced significant amounts of reflected rays with polar angles of less than 90° are circled for additional emphasis.

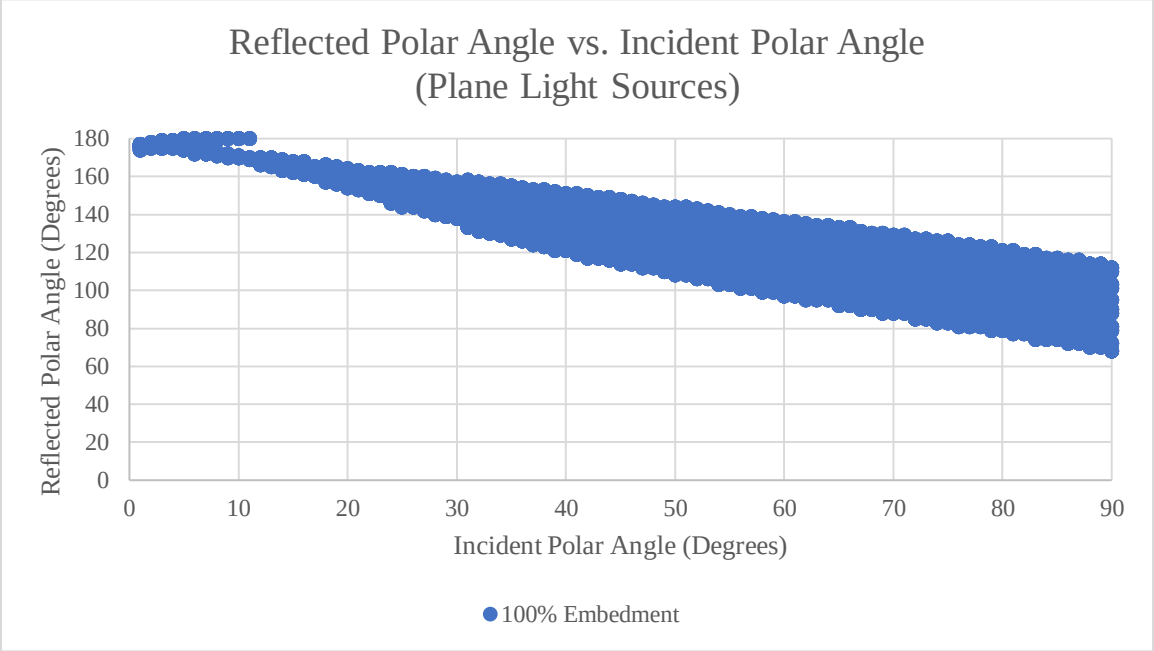

Figure 42: Optical simulations plane light source angle relationships (100% embedment).

The plane light source simulations at 100% embedment (Figure 42) produced reflected rays as approximately predicted by the Law of Reflection. Reflected rays were observed at polar angles supplementary to the incident polar angles, with spread distributions corresponding to the area of the plane light source when projected onto the simulated roadway marking surface. These results match those predicted by electromagnetic interface theory, as the modeled roadway marking binder behaved as an ideal reflector.

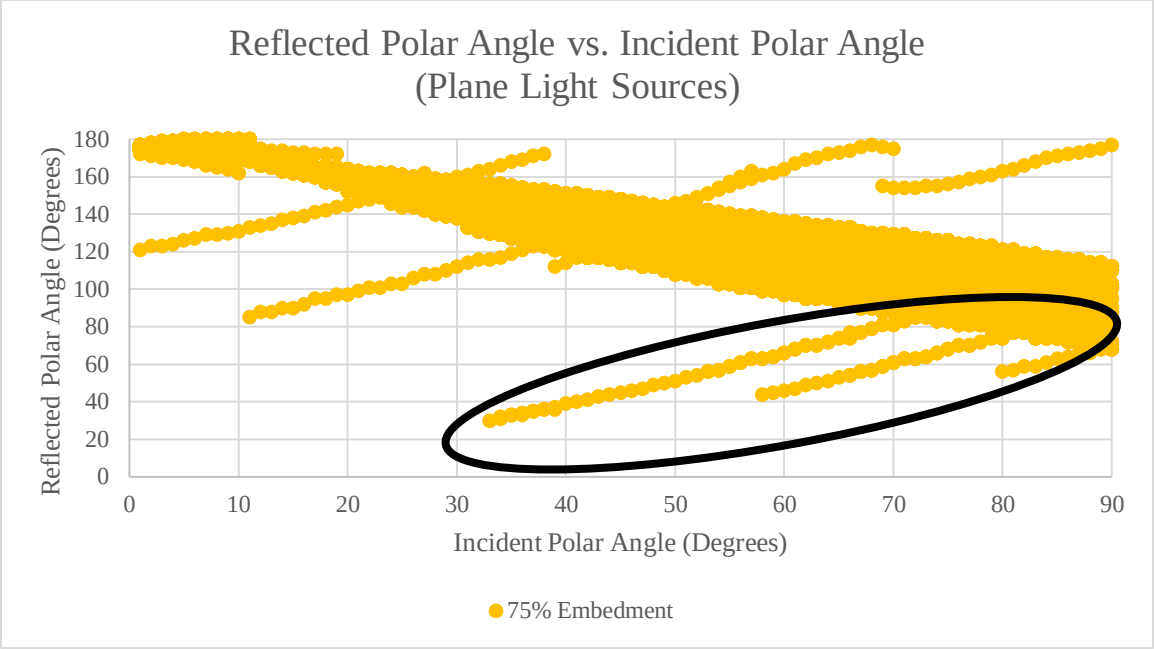

Figure 43: Optical simulations plane light source angle relationships (75% embedment).

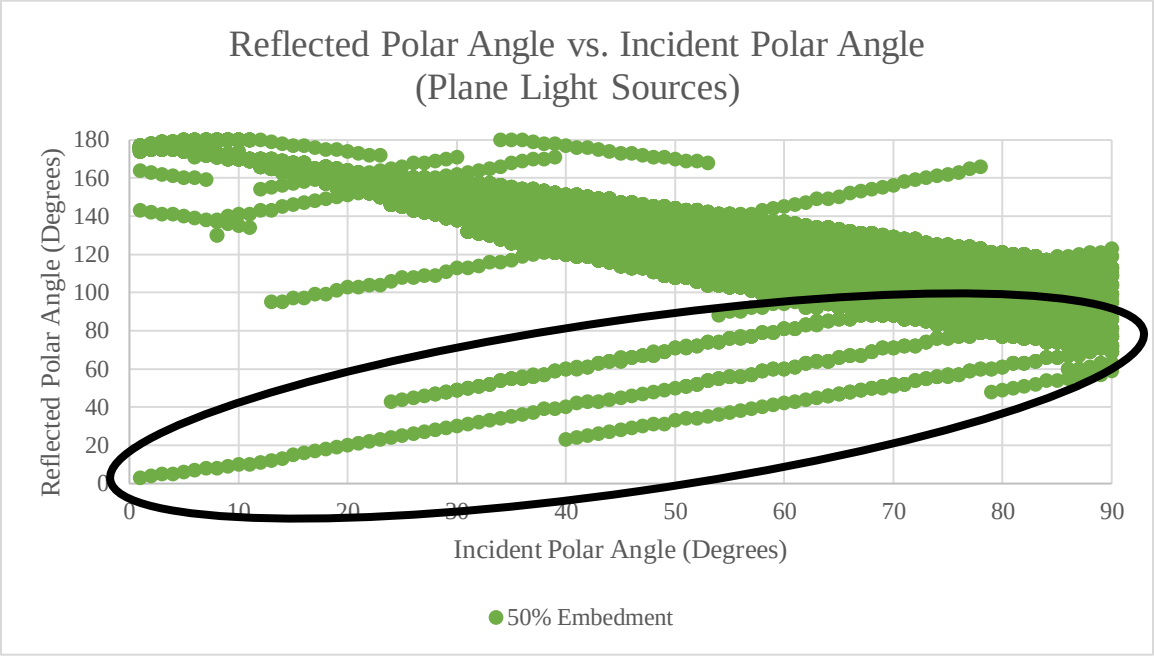

Figure 44: Optical simulations plane light source angle relationships (50% embedment).

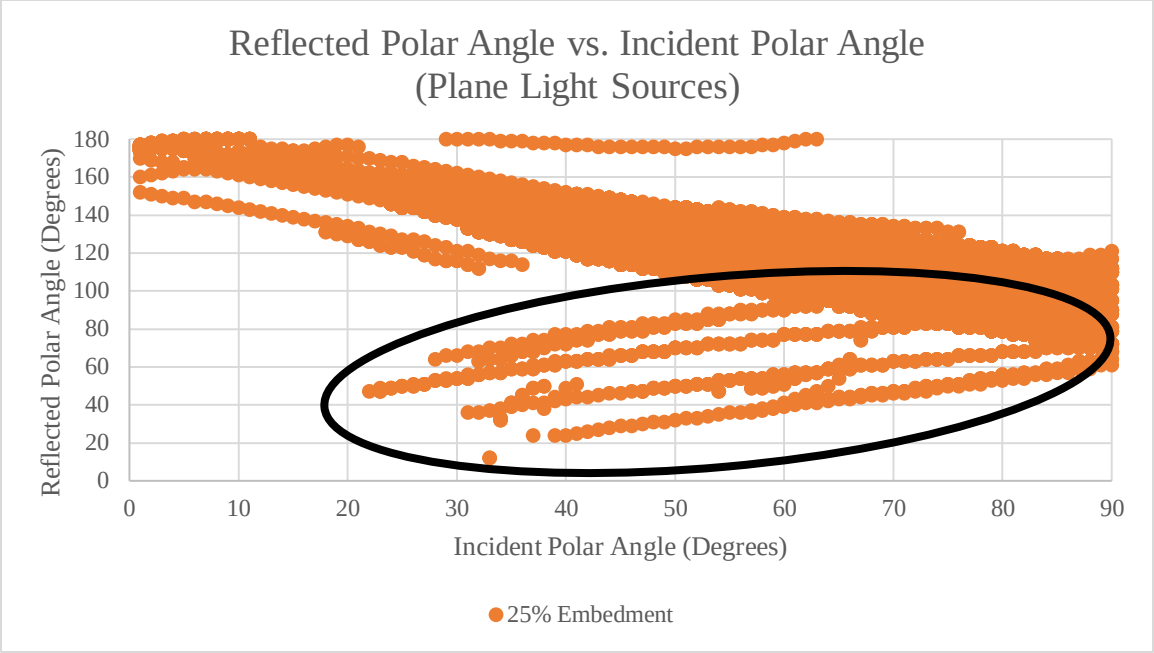

Figure 45: Optical simulations plane light source angle relationships (25% embedment).

The plane light source simulations at 75% embedment (Figure 43), 50% embedment (Figure 44), and 25% embedment (Figure 46) produced reflected rays similarly to the simulations at 100% embedment, as many of the incident rays only interacted with the simulated roadway marking binder. Interactions with the glass bead produced additional reflections at other polar angles for all three sets of simulations however, including true retroreflections for incident polar angles greater than 33° at 75% embedment and all incident polar angles at 50% embedment.

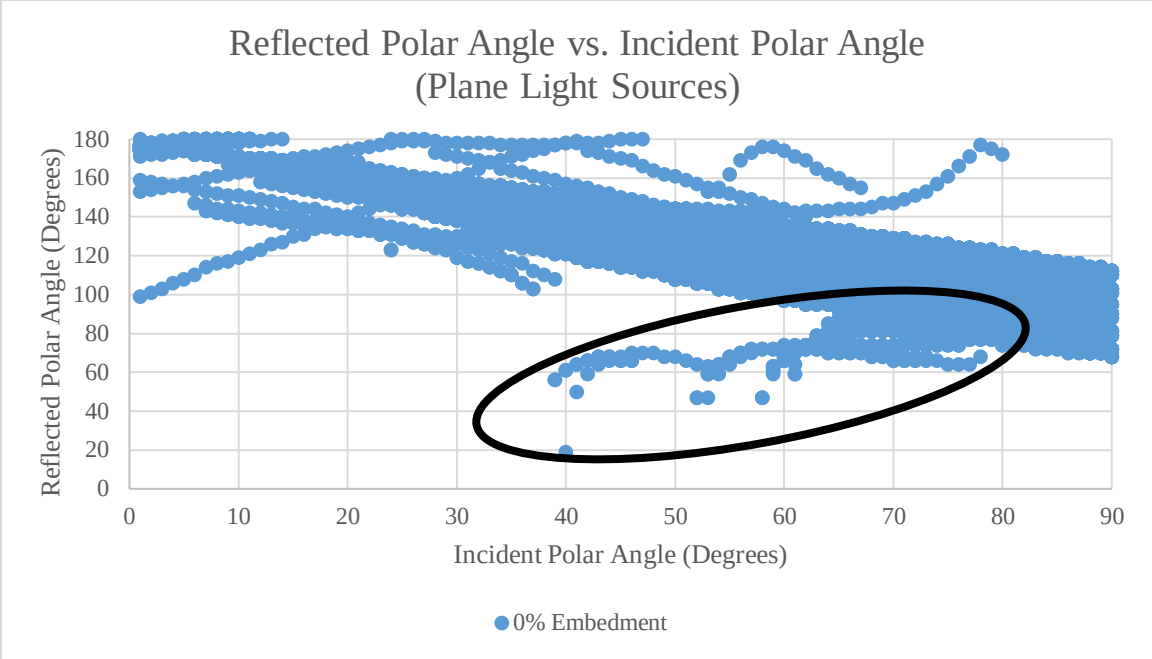

Figure 46: Optical simulations plane light source angle relationships (0% embedment).

The plane light source simulations at 0% embedment (Figure 46) produced reflected rays at various polar angles not predicted by the Law of Reflection as well, but it should be noted that very few glass beads at 0% embedment are typically present on real roadway markings, as glass beads at low embedment levels do not adhere well to most roadway marking binders [3]. The simulated data therefore suggests that a roadway marking machine vision system will measure large signal intensities when the light source and optical imager are positioned at equal polar angles relative to the target, with the greatest signal intensities being expected when both polar angles are 90°.

8. Machine Vision Imaging Experiments

These experiments were performed in order to experimentally confirm the simulation results detailed in Section 7.3 by investigating the relationship between the reflective properties of composite roadway markings and the respective polar angles of the light source and optical imager components of a machine vision system. A light source (high power, multi-color LEDs) and an optical imager (charge-coupled device (CCD) camera) were fixed at several independently varying polar angles (θ_1 and θ_2 respectively) within a plane of incidence that included a target (roadway marking sample), as was described in Section 7 and shown in Figure 34.

For three different targets (a white roadway marking sample with embedded glass beads, a yellow roadway marking sample with embedded glass beads, and a sheet of black tar paper), broad spectrum white light was emitted from the light source and the reflected radiation was captured in a digital image by the optical imager. This process was performed with the optical imager fixed at varied polar angles of 30°, 60°, and 90° while the light source was fixed at varied polar angles of 30°, 60°, 90°, 120°, and 150°.

For each captured grayscale digital image, the region corresponding to the imaged target was identified and spatially filtered. Average pixel intensity values for the identified region were then calculated and compared to the same region of the black tar paper target, which acted as a control for these experiments. These normalized pixel intensity values were then used to determine the relationship between the optical imager and light source polar angles and the resulting machine vision image signal intensity.

8.1. Experimental Setup

Two epoxy roadway marking samples were used as targets in these experiments. Both samples were applied from a standard roadway striping vehicle onto plywood boards so that the samples could be transported for testing purposes. Type A and Type B glass beads were dispensed onto these samples in accordance with PennDOT regulations regarding epoxy roadway markings. Black tar paper was used to cover all portions of the plywood boards not covered by the applied binder as shown in Figure 47, as the tar paper can be expected not to reflect significant amounts of electromagnetic radiation in the visible spectrum. The boards were covered such that the exposed surface areas of both binder samples were approximately equal.

Figure 47: White (left) and yellow (right) roadway marking samples (with glass beads).

A LED Engin LuxiGen LZ7-04MU00 multi-color LED package was used as a light source in these experiments, as it was also used in the experiments detailed in Section 6. The package is shown in Figure 29. For these experiments, only the broad

spectrum white LED was used as a light source, with a maximum luminous flux of 255 lumens and a correlated color temperature (CCT) of 65000 Kelvin. The spectral distribution of the white LED is shown in Figure 48 (adapted from [25]).

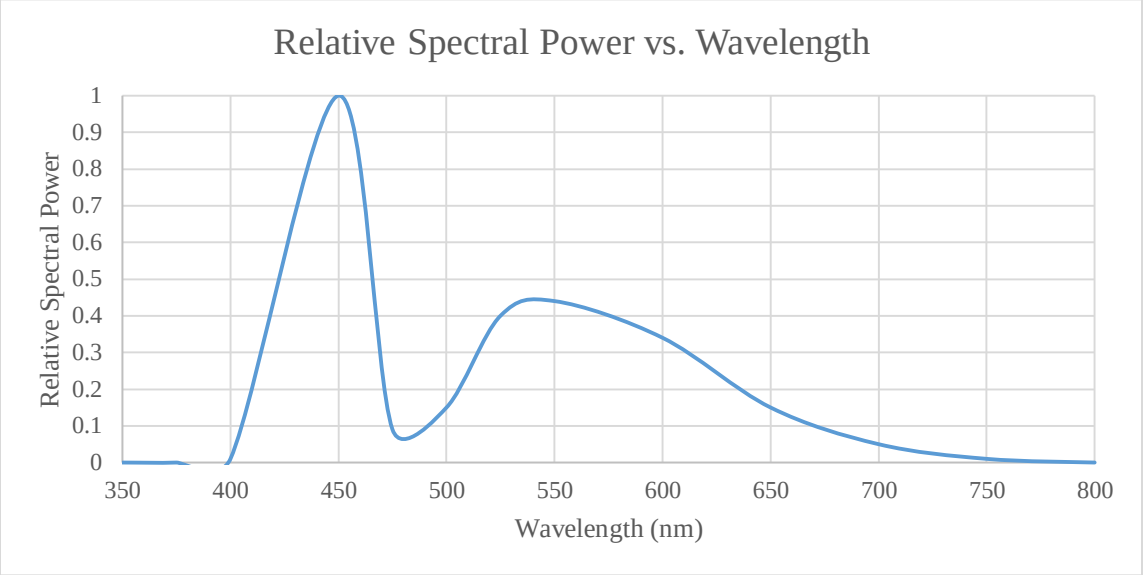

Figure 48: LED Engin LuxiGen LZ7-04MU00 package white LED spectral distribution.

A plywood arc was constructed for the purpose of securing the light source and optical imager at independent polar angles with respect to the target as shown in Figure 49. The arc was constructed such that the light source and optical imager could be mounted along a plane at polar angles ranging from 0° to 180° with a fixed radial distance of 1.0 meter. A separating barrier was included in the midsection of the arc so that radiation emitted from the light source could not reach the optical imager without first being reflected from the target.

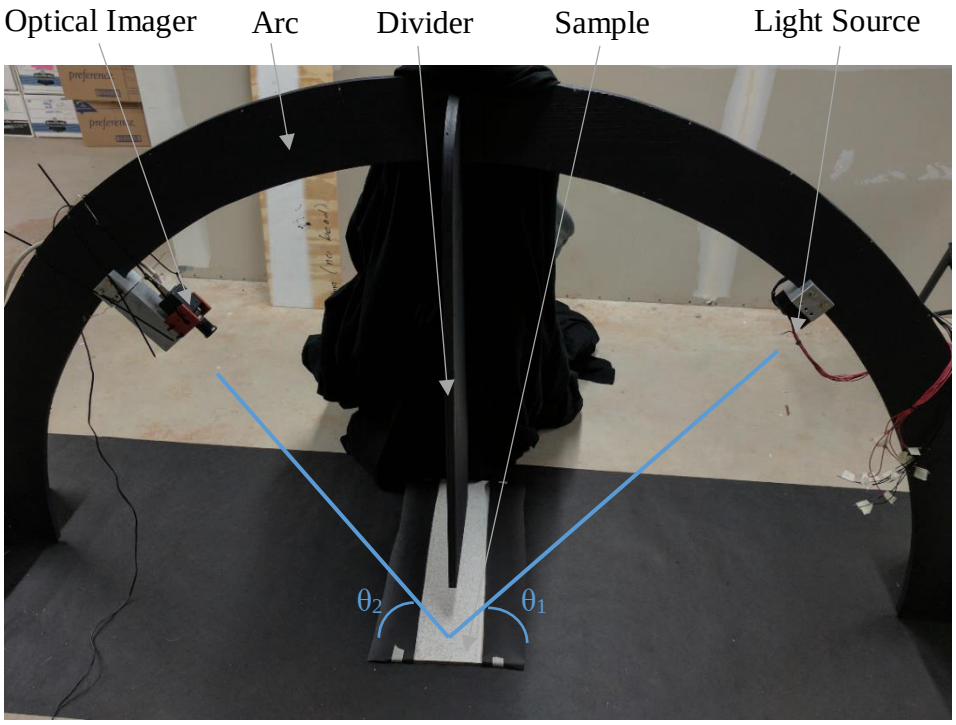

Figure 49: Plywood arc with mounted CCD camera and light source.

8.2. Measurement Instrumentation

A JAI TM-6740 CL CCD camera was used as an optical imager in these experiments. The camera was mounted on the arc at the various described polar angles as shown in Figure 50 with the aperture of the camera directed towards the target. Various technical specifications for the camera are included in Table 8 [26].

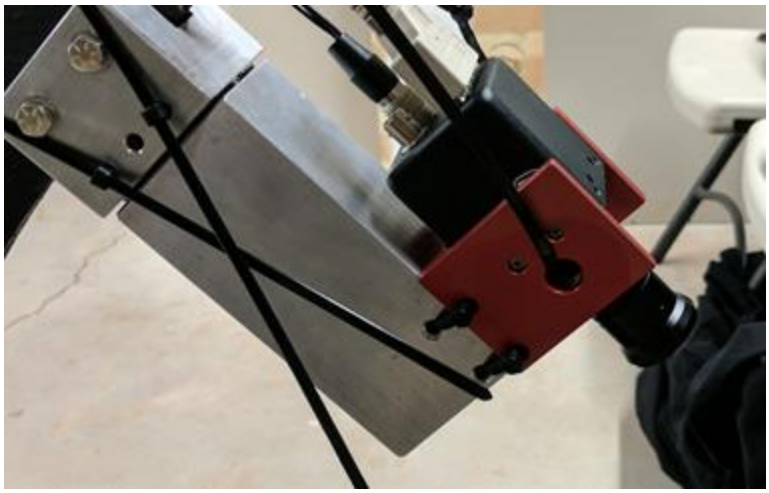

Figure 50: JAI RM-6740CL CCD camera.

Table 8: JAI TM-6740 CL CCD Camera Select Specifications

Parameter	Specification
Sensor	1/3” progressive scan interline transfer CCD
Active Area	4.74 mm x 3.55 mm
Active Pixels	640 x 480
Signal-to-Noise Ratio	> 50 dB
Lens Mount	C-Mount

Additionally, the approximate spectral responsivity of the camera is shown in Figure 51. The JAI TM-6740 CL CCD camera captures monochromatic images weighted by a single spectral responsivity curve [26].

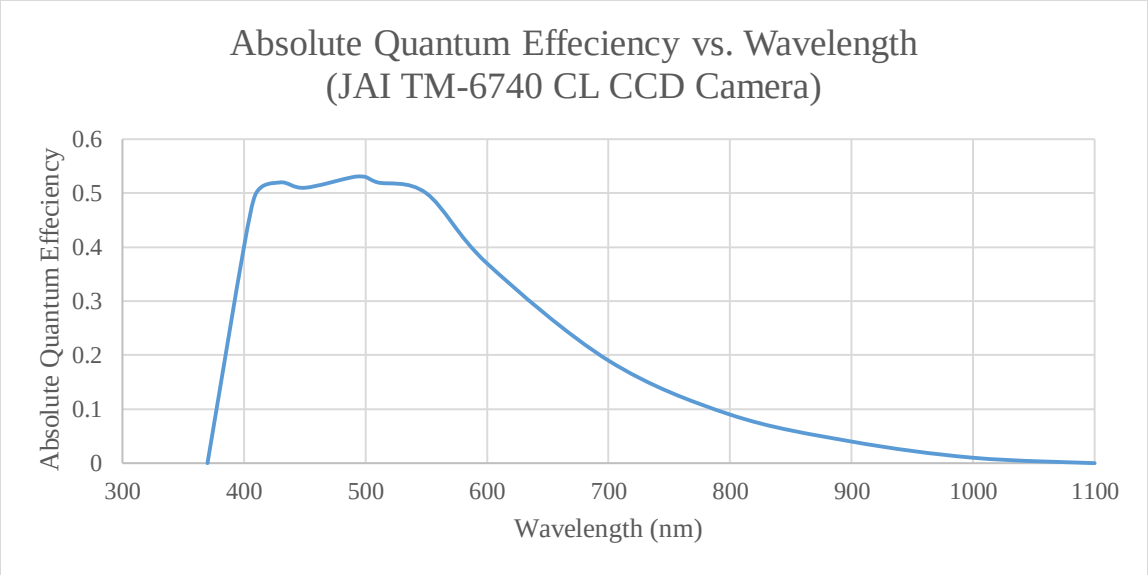

Figure 51: JAI TM-6740 CL CCD camera spectral responsivity.

The camera was equipped with a Fujinon TF2.8DA-8 lens. The aperture of the lens was at full open for the duration of these experiments, with the lens focused such that the clarity of the captured images was maximized. Various technical specifications for the lens are included in Table 9 [27].

Table 9: Fujinon TF2.8DA-8 Lens Select Specifications

Parameter	**Specification**
Focal Length	2.86 mm
Aperture	2.2 mm
Back Focal Distance	14.51 mm
Distortion	-6.25%
Relative Illumination (at diagonal image height)	51

8.3. Results and Analysis

Experimental results are summarized in scatter plots for imager polar angles of 30°, 60°, and 90° as shown in Figure 52, Figure 53, and Figure 54 respectively. Captured images were represented as bit arrays, with pixel light intensity values ranging from 0 to 255. The region of each image corresponding to the target was identified and spatially filtered using MathWorks MATLAB software, with the reflected light intensity values being the average of the filtered pixel values in the identified region. The values were then normalized by taking the ratio of the reflected light intensity values associated with each roadway marking target and the reflected light intensity values associated with the black tar paper target for each given geometric configuration. Raw measurements are included in Appendix D.

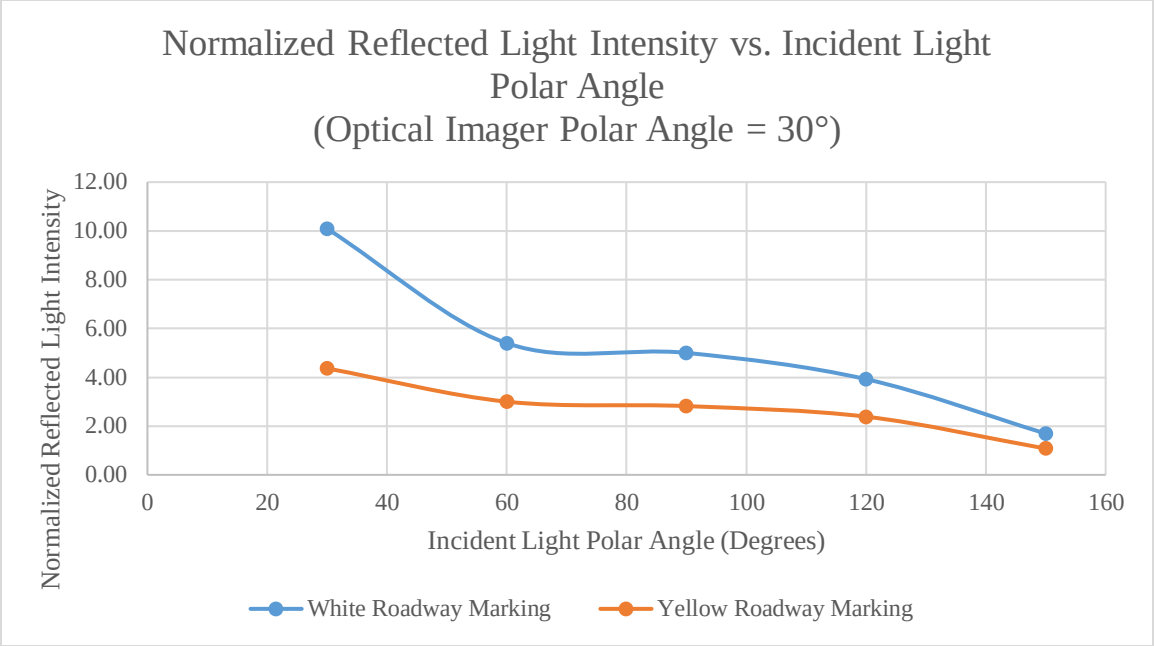

Figure 52: Machine vision imaging measured reflected light intensities (optical imager polar angle = 30°).

In the experiments performed with the optical imager at a polar angle of 30° (Figure 52), the highest reflected light intensities were measured when the light source was positioned at a polar angle of 30° for both the white and yellow roadway marking targets. Normalized reflected light intensity values indicate that the samples produced 10.1 and 4.4 times the reflected light intensity of the black tar paper target respectively in the described configuration, with reflected light intensities decreasing as the incident light polar angle was increased. These results agree with the theoretical results detailed in Section 7.3, which indicate that a light source and optical imager positioned at the same polar angle relative to the target should produce the largest signal intensity.

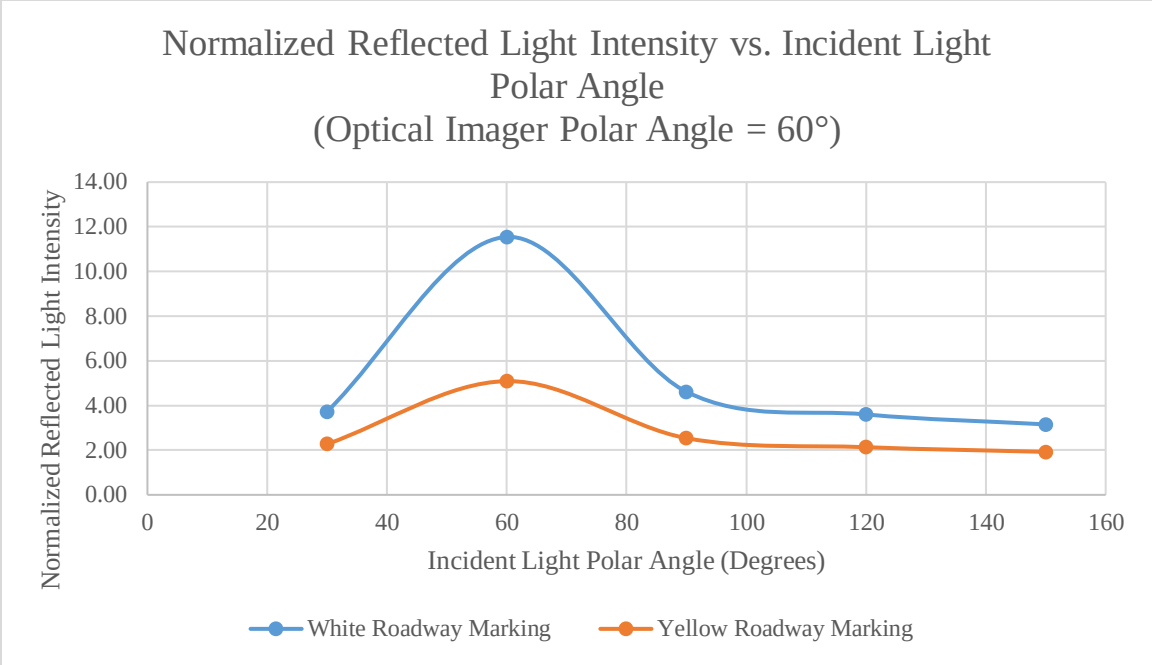

Figure 53: Machine vision imaging measured reflected light intensities (optical imager polar angle = 60°).

In the experiments performed with the optical imager at a polar angle of 60° (Figure 53), the highest reflected light intensities were measured when the light source was positioned at a polar angle of 60° for both the white and yellow roadway marking targets. Normalized reflected light intensity values indicate that the samples produced 11.6 and 5.1 times the reflected light intensity of the black tar paper target respectively in the described configuration, with reflected light intensities decreasing as the incident light polar angle was either increased or decreased from 60°. These results also agree with the theoretical results detailed in Section 7.3.

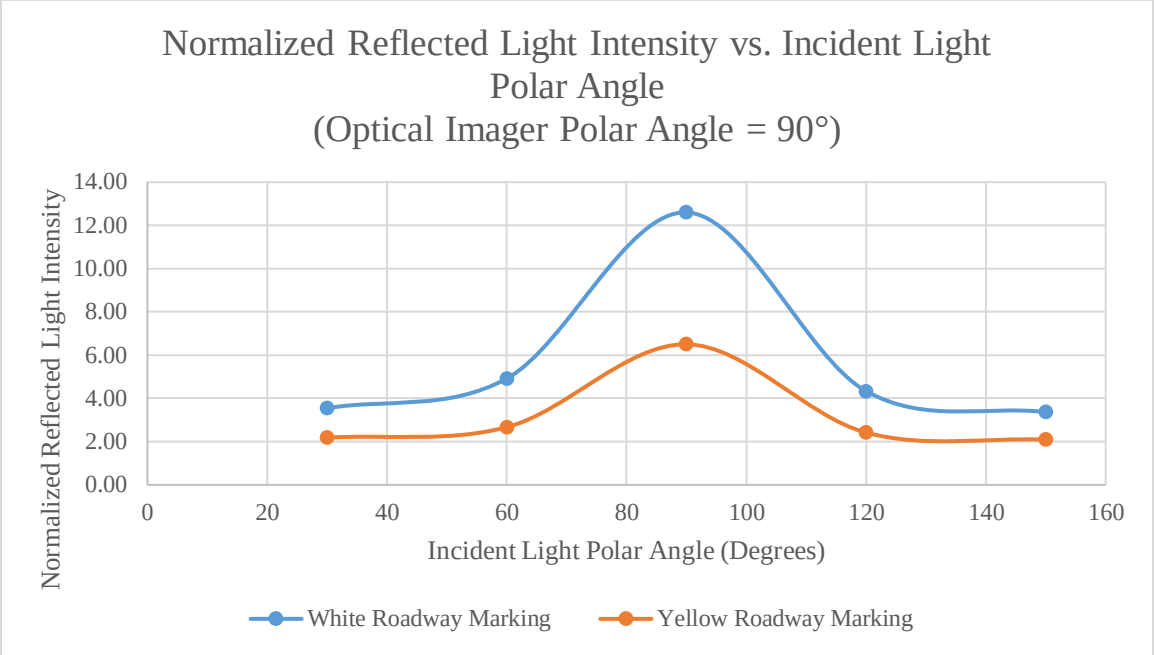

Figure 54: Machine vision imaging measured reflected light intensities (optical imager polar angle = 90°).

In the experiments performed with the optical imager at a polar angle of 90° (Figure 54), the highest reflected light intensities were measured when the light source was positioned at a polar angle of 90° for both the white and yellow roadway marking targets. Normalized reflected light intensity values indicate that the samples produced 12.6 and 6.5 times the reflected light intensity of the black tar paper target respectively in the described configuration, with reflected light intensities decreasing as the incident polar angle was either increased or decreased from 90°. These results also agree with the theoretical results detailed in Section 7.3.

It is important to note that the maximum reflected light intensity values measured in these experiments increased as the polar angle of the optical imager was increased to 90°, with the highest values being measured when the optical imager was positioned at

exactly 90°. This result agrees with the theoretical results detailed in Section 7.4, which indicate that the highest reflected light intensities should be measured when the light source and optical imager are positioned at polar angles of 90°. Additionally, it is also important to note that the yellow roadway marking sample consistently produced lower reflected light intensities than the white roadway marking sample. This result agrees with the experimental results detailed in Section 6.3, which indicate that white roadway marking binders exhibit higher reflectivity across the visible spectrum, therefore producing reflected electromagnetic waves with higher intensities in the visible spectrum.

9. Conclusion

Using the experimental and theoretical procedures detailed in this work, results pertaining to several important optical characteristics of roadway markings were obtained. In the design of any machine vision system for the imaging of roadway markings, the implications of these results must be considered in order to maximize the reflected signal intensity acquired by the system. This is highly desirable, as a large signal-to-noise ratio will increase the efficacy of the detection algorithms used to process the captured images, thereby increasing the detection reliability of the overall machine vision system.

The specific findings of this work are as follows:

- For a properly applied roadway marking (where glass bead rolling effects have been minimized), the reflective properties of the marking do not depend upon the azimuthal angle of observation when observed within 30-meter geometry;

- A typical white roadway marking will exhibit approximately consistent reflectivity across the visible spectrum, while a typical yellow roadway marking will exhibit lower reflectivity for smaller visible wavelengths (suggesting that light sources emitting yellow or red wavelengths may produce higher reflected signal intensities when imaging roadway marking targets);

- For a machine vision system in a planar geometric configuration, higher reflected signal intensities will be measured when the light source and optical imager are positioned at the same polar angle relative to the roadway marking target; and

- For a machine vision system, the highest reflected signal intensity will be measured when the light source and optical imager are positioned at polar angles of 90° relative to the roadway marking target.

While these findings certainly must be considered in the design of machine vision systems for imaging roadway markings, future work is still required in order to fully optimize these systems to maximize their reflected signal intensities. Non-planar geometric machine vision system configurations must be studied, for example, to determine if any configurations other than those mentioned in this work might result in high reflected signal intensity as well. More precise roadway marking binder reflection characteristics (including any possible unique responses to polarized incident radiation) must also be experimentally determined, in order to more precisely optimize machine vision light sources.

Additional necessary studies include a comprehensive optical analysis of various pavements so that measured reflected signal intensities from the surfaces surrounding roadway markings can be minimized. While this work primarily focuses on increasing reflected signal intensity from roadway markings as a means to increase the overall reflected signal intensity, decreasing reflections from surrounding pavements would

improve a system's ability to accurately image roadway markings as well. Studies addressing the effects of the presence of common outdoor substances (moisture, dirt, etc.) on all of the aforementioned optical properties would also be prudent, as those substances may very well be present when the described machine vision systems are operating in the field.

References

[1] A. B. Hillel, R. Lerner, D. Levi and G. Raz, "Recent Progress in Road and Lane Detection: A Survey," *Machine Vision and Applications,* vol. 25, no. 3, pp. 727-745, 2014.

[2] C. C. Rhodes and B. W. Pocock, "A Discussion of the Principles of Glass Bead Reflectorization," Michigan State Highway Department, 1951.

[3] M. Reckinger, "The Visibility of Road Markings by Night: A Presentation on the Principles of Reflectorising Road Markings," Potters Ballotini Europe, 1981.

[4] K. Vedam and M. D. Stoudt, "Retroreflection from spherical glass beads in highway pavement markings. 2: Diffuse reflection (a first approximation calculation)," *Applied Optics,* vol. 17, no. 12, pp. 1859-1869, 1978.

[5] USDOT Federal Highway Administration, "Manual on Uniform Traffic Control Devices (MUTCD)," United States Department of Transportation, 2015.

[6] R. G. McGinnis, "Pavement Markings Benchmarking," *No. FHWAPA-2001-027-97-04,* 2002.

[7] VDOT, "2008 Pavement Marking Certification Study Guide," Virginia Department of Transportation, Richmond, VA, 2008.

[8] Guidemark Inc., *Magnified Road Mark Images,* Souderton, PA, 2016.

[9] European Committee for Standardization (CEN), *CEN EN 1436 Road Marking Materials - Road Marking Performance for Road Users,* 2007.

[10] ASTM International, *Standard Test Method for Measurement of Retroreflective Pavement Marking Materials with CEN-Prescribed Geometry Using a Portable Retroreflectometer,* 2011.

[11] Delta, *LTL-X Retrometer Manual (Rev. 15),* 2012.

[12] K. Matković, *Tone Mapping Techniques and Color Image Difference in Global Illumination,* Eurographics Digital Library, 1997.

[13] W. N. Craig, W. Sitzabee, W. Rasdorf and J. Hummer, "Statistical validation of the effect of lateral line location on pavement marking retroreflectivity degradation," *Public Works Management & Policy,* vol. 12, no. 2, pp. 431-450, 2007.

[14] O. Smadi, N. Hawkins, B. Aldemir-Bektas, P. Carlson, A. Pike and C. Davies, "Recommended Laboratory Test for Predicting the Initial Retroreflectivity of Pavement Markings from Glass Bead Quality," pp. 94-102, 2014.

[15] USDOT Federal Highway Administration, *Standard Specifications for Construction of Roads and Bridges on Federal Highway Projects.*

[16] PennDOT, "1103.14 Reflective Glass Beads," in *Specifications Publication 408/2000*, Commonwealth of Pennsylvania Department of Transportation.

[17] PennDOT, "Section 962 - Waterborne Pavement Markings," in *Specifications Publication 408/2000*, Commonwealth of Pennsylvania Department of Transportation.

[18] PennDOT, "Section 964 - Epoxy Pavement Markings," in *Specifications Publication 408/2000*, Commonwealth of Pennsylvania Department of Transportation.

[19] PennDOT, "Section 960 - Hot Thermoplastic Pavement Markings," in *Specifications Publication 408/2000*, Commonwealth of Pennsylvania Department of Transportation.

[20] M. Pellerite, S. Clear, C. Elsbernd and R. Flynn, "Optical Elements Comprising a Polyfluoropolyether Surface Treatment". United States of America Patent US6632508 B1, 14 October 2003.

[21] W. Rasdorf, G. Zhang and J. Hummer, "The Impact of Directionality on Paint Pavement Marking Retroreflectivity," *Public Works Management & Policy,* vol. 13, no. 3, pp. 267-277, 2009.

[22] K. Hall, C. Davies, T. Still, K. Wolos and K. Grimbilas, "Highway Marking Sphere Dispensing Apparatus". United States of America Patent US7654770 B2, 2 February 2010.

[23] E. Hecht, Optics, 4th ed., Reading, MA: Addison-Wesley, 2002.

[24] C. Starr, C. Evers and L. Starr, Biology: Concepts and Applications, Thomson Brooks/Cole, 2006.

[25] LED Engin, *LuxiGen Multi-Color Emitter Series (LZ7-04MU00)*, 2016.

[26] JAI, *TM-6740 CL / TMC-6740 CL (Progressive Scan CCD).*

[27] Fujinon, *For FA/Machine Vision 3CCD Camera.*

[28] CIE, *International Lighting Vocabulary*, 4th ed., 1987.

[29] M. Riedl, Optical Design Fundamentals for Infrared Systems, 2nd ed., Bellingham, Washington: SPIE Press, 2001.

Appendix A: Electromagnetic Interface Derivations

The geometric relationships formed between the incident, reflected, and transmitted rays at an electromagnetic interface can be modeled through the application of Fermat's Principle, which states that a light ray traveling between two points will always take the path that can be traversed in the least time [23]. Also inherent in the following derivations are the assumptions that the interface is approximately flat and the material properties are approximately uniform near the interface.

In Figure 12, the time required for a light ray to travel from point A to point C ($t_{A\to C}$) is dependent upon lengths $\overline{AO}$ and $\overline{OC}$, as well the phase velocities of light for the incident and transmitted rays ($v_{p,i}$ and $v_{p,t}$ respectively) as shown in Equation 22.

$$t_{A\to C} = t_{A\to O} + t_{O\to C} = \frac{\overline{AO}}{v_{p,i}} + \frac{\overline{OC}}{v_{p,t}} \qquad (22)$$

The described path is shown in Figure 55. Lengths x, y, a, and b are included in the figure for reference purposes.

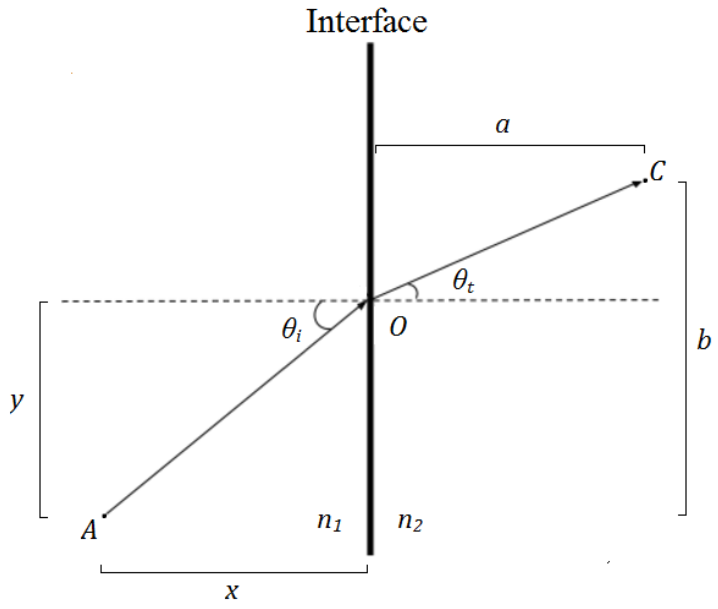

Figure 55: Modified electromagnetic interface diagram (transmission only).

In reference to Figure 55, Equation 22 can be rewritten using the Pythagorean Theorem as shown in Equation 23.

$$t_{A\to C} = \frac{\overline{AO}}{v_{p,i}} + \frac{\overline{OC}}{v_{p,t}} = \frac{\sqrt{x^2+y^2}}{v_{p,i}} + \frac{\sqrt{a^2+(b-y)^2}}{v_{p,t}} \qquad (23)$$

In order to minimize $t_{A\to C}$ with respect to variations in y (as necessitated by Fermat's Principle), the spatial derivative of $t_{A\to C}$ must be equal to 0 as shown in Equation 24.

$$\frac{dt_{A\to C}}{dy} = \frac{y}{v_{p,i}\sqrt{x^2+y^2}} + \frac{-(b-y)}{v_{p,t}\sqrt{a^2+(b-y)^2}} = 0 \qquad (24)$$

In reference to Figure 55, Equation 24 can be rewritten using trigonometric relationships as shown in Equation 25. The equation can then be further rewritten as shown in Equation 26.

$$\frac{dt_{A\to C}}{dy} = \frac{sin\,\theta_i}{v_{p,i}} + \frac{-\,sin\,\theta_t}{v_{p,t}} = 0 \qquad (25)$$

$$\frac{sin\,\theta_i}{v_{p,i}} = \frac{sin\,\theta_t}{v_{p,t}} \qquad (26)$$

Using Equation 2, substitutions can be made for $v_{p,i}$ and $v_{p,t}$ as shown in Equation 27. Both expressions can then be reduced as shown in Equation 28. The derived relationship shown in Equation 28 is Snell's Law, which relates θ_t to θ_i.

$$\frac{n_1}{c} sin\,\theta_i = \frac{n_2}{c} sin\,\theta_t \qquad (27)$$

$$n_1\,sin\,\theta_i = n_2\,sin\,\theta_t \qquad (28)$$

This relationship can also be used to relate θ_r to θ_i as well when it is recognized that the incident ray and reflected ray both propagate through the same material (which is assumed to be approximately uniform in this model). For this case, Equation 28 can be rewritten as shown in Equation 29. This relationship is further simplified in Equation 30 to conclude the derivation of the Law of Reflection, which relates θ_r to θ_i.

$$n \sin \theta_i = n \sin \theta_r \quad (29)$$

$$\theta_i = \theta_r \quad (30)$$

Once the geometric bearings of the produced rays have been considered, it is also important to consider the proportions of the incident ray energy that become associated with the transmitted and reflected rays respectively. The sum of the energies associated with the transmitted and reflected rays produced from an electromagnetic interface interaction is equal to the energy associated with the incident ray. These proportions can be found by considering the concepts of reflectivity and transmissivity, which are properties related to several relevant material properties of the regions on either side of the electromagnetic interface.

In order to obtain formal definitions for reflectivity and transmissivity, considerations must be made for the electric field intensity ($\vec{\boldsymbol{E}}$) and magnetic flux density ($\vec{\boldsymbol{B}}$) associated with each light ray in a geometric optical model. Specifically, it must be noted that for each light ray traveling in a specified direction ($\hat{\boldsymbol{k}}$) as shown in Figure 12, associated electric and magnetic fields exist such that $\vec{\boldsymbol{E}} \cdot \vec{\boldsymbol{B}} = 0$ (the fields are perpendicular to each other). Additionally, it must be noted that the electric field intensity and magnetic flux density can be related as shown in Equation 31, the magnetic flux density that is normal to an electromagnetic interface must be continuous across that interface as shown in Equation 32 (assuming all involved materials are dielectrics as in

this model), and the electric field intensity that is parallel to an electromagnetic interface must be continuous across that interface as shown in Equation 33 [23].

$$\widehat{\boldsymbol{k}}\times\vec{\boldsymbol{E}} = v_p\vec{\boldsymbol{B}} \tag{31}$$

$$\vec{\boldsymbol{B}}_{1,\perp} = \vec{\boldsymbol{B}}_{2,\perp} \tag{32}$$

$$\vec{\boldsymbol{E}}_{1,\parallel} = \vec{\boldsymbol{E}}_{2,\parallel} \tag{33}$$

It is also necessary to consider the components of the combined fields in each material that are polarized in the direction parallel to the interface (such that $\widehat{\boldsymbol{k}}\cdot\vec{\boldsymbol{E}} = 0$) and normal to the interface (such that $\widehat{\boldsymbol{k}}\cdot\vec{\boldsymbol{B}} = 0$). Any incident, reflected, or transmitted electromagnetic wave can be separated into the two described components.

For the parallel-polarized components of the waves, the magnitudes of the incident, reflected, and transmitted magnetic flux densities ($B_{0,i}$, $B_{0,r}$, and $B_{0,t}$ respectively) can be related using Equation 32 as shown in Equation 34.

$$-B_{0,i}\cos\theta_i + B_{0,r}\cos\theta_r = -B_{0,t}\cos\theta_t \tag{34}$$

As the electric field intensities and magnetic flux densities are normal to their corresponding counterparts, Equation 34 can be rewritten using Equation 31 as shown in Equation 35.

$$-\frac{E_{0,i}}{v_{p,i}} cos\,\theta_i + \frac{E_{0,r}}{v_{p,r}} cos\,\theta_r = -\frac{E_{0,t}}{v_{p,t}} cos\,\theta_t \qquad (35)$$

Using Equation 30 and noting that $v_{p,i} = v_{p,r}$ (as shown in Equation 2, given that both the incident and reflected waves travel in the same medium), Equation 35 can be rewritten as shown in Equation 36.

$$\frac{1}{v_{p,i}}\left(E_{0,i} - E_{0,r}\right) cos\,\theta_i = \frac{1}{v_{p,t}} E_{0,t}\, cos\,\theta_t \qquad (36)$$

Using Equation 2, Equation 36 can be further rewritten as shown in Equation 37.

$$n_1\left(E_{0,i} - E_{0,r}\right) cos\,\theta_i = n_2 E_{0,t}\, cos\,\theta_t \qquad (37)$$

The combined use of Equation 37 and Equation 33 allows for the expression of the parallel amplitude reflection coefficient ($r_{\parallel}$) and parallel amplitude transmission coefficient ($t_{\parallel}$), which are defined as ratios of electric field intensities as shown in Equation 38 and Equation 39 respectively [23].

$$r_{\parallel} = \left(\frac{E_{0,r}}{E_{0,i}}\right)_{\parallel} = \frac{n_1 \cos\theta_i - n_2 \cos\theta_2}{n_1 \cos\theta_i + n_2 \cos\theta_2} \quad (38)$$

$$t_{\parallel} = \left(\frac{E_{0,t}}{E_{0,i}}\right)_{\parallel} = \frac{2n_1 \cos\theta_i}{n_1 \cos\theta_i + n_2 \cos\theta_2} \quad (39)$$

Similarly, for the normal-polarized components of the waves, the magnitudes of the incident, reflected, and transmitted electric field intensities (E_i, E_r, and E_t respectively) can be related using Equation 33 as shown in Equation 40.

$$E_{0,i} \cos\theta_i - E_{0,r} \cos\theta_r = E_{0,t} \cos\theta_t \quad (40)$$

As the components of the magnetic flux densities normal to the interface are continuous across the interface (as shown in Equation 32), Equation 40 can be rewritten using Equation 31 as shown in Equation 41.

$$\frac{E_{0,i}}{v_{p,i}} \cos\theta_i + \frac{E_{0,r}}{v_{p,r}} \cos\theta_r = \frac{E_{0,t}}{v_{p,t}} \cos\theta_t \quad (41)$$

Using Equation 30 and noting that $v_{p,i} = v_{p,r}$ (as shown in Equation 2, given that both the incident and reflected waves travel in the same medium), Equation 41 can be rewritten as shown in Equation 42.

$$\frac{1}{v_{p,i}}\left(E_{0,i}+E_{0,r}\right)cos\,\theta_i=\frac{1}{v_{p,t}}E_{0,t}\,cos\,\theta_t \quad (42)$$

Using Equation 2, Equation 42 can be further rewritten as shown in Equation 43.

$$n_1\left(E_{0,i}+E_{0,r}\right)cos\,\theta_i=n_2E_{0,t}\,cos\,\theta_t \quad (43)$$

The combined use of Equation 43 and Equation 33 allows for the expression of the normal amplitude reflection coefficient ($r_\perp$) and normal amplitude transmission coefficient ($t_\perp$), which are defined as ratios of electric field intensities as shown in Equation 44 and Equation 45 respectively [23].

$$r_\perp=\left(\frac{E_{0,r}}{E_{0,i}}\right)_\perp=\frac{n_2\,cos\,\theta_i-n_1\,cos\,\theta_t}{n_2\,cos\,\theta_i+n_1\,cos\,\theta_t} \quad (44)$$

$$t_\perp=\left(\frac{E_{0,t}}{E_{0,i}}\right)_\perp=\frac{2n_1\,cos\,\theta_i}{n_2\,cos\,\theta_i+n_1\,cos\,\theta_t} \quad (45)$$

With both sets of reflection and transmission coefficients properly defined, it is possible to formally derive expressions for reflectance and transmittance (and ultimately reflectivity and transmissivity). Both material properties can be expressed in terms of electromagnetic radiant flux density (I), which is defined as shown in Equation 46 (for isotropic media) with ϵ being the electric permittivity of the medium in which the wave is traveling. Each incident, reflected, and transmitted electromagnetic wave will have an

associated radiant flux density (I_i, I_r, and I_t respectively). This value is typically expressed in Watts per square meters.

$$I = \frac{1}{2} v_p \epsilon {E_0}^2 \quad (46)$$

Reflectance and transmittance can therefore be defined by focusing on an arbitrary area (A) of the interface shown in Figure 12. Reflectance (R) is defined as the ratio of the reflected power through A to the incident power through A as shown in Equation 47, and transmittance (T) is defined as the ratio of the transmitted power through A to the incident power through A as shown in Equation 48.

$$R = \frac{I_r A \cos \theta_r}{I_i A \cos \theta_i} \quad (47)$$

$$T = \frac{I_t A \cos \theta_t}{I_i A \cos \theta_i} \quad (48)$$

After canceling both A terms, Equation 30 can be used to simplify Equation 47 as shown in Equation 49.

$$R = \frac{I_r A \cos \theta_r}{I_i A \cos \theta_i} = \frac{I_r \cos \theta_i}{I_i \cos \theta_i} = \frac{I_r}{I_i} \quad (49)$$

Equation 49 can be further modified using Equation 46 as shown in Equation 50, with ϵ_1 and ϵ_2 denoting the electric permittivities of Region 1 and Region 2 respectively.

$$R = \frac{I_r}{I_i} = \frac{\frac{1}{2}v_{p,r}\epsilon_1 {E_{0,r}}^2}{\frac{1}{2}v_{p,i}\epsilon_1 {E_{0,i}}^2} = \frac{\frac{1}{2}v_{p,r}\epsilon_1 {E_{0,r}}^2}{\frac{1}{2}v_{p,r}\epsilon_1 {E_{0,i}}^2} = \left(\frac{E_{0,r}}{E_{0,i}}\right)^2 = \left(\left(\frac{E_{0,r}}{E_{0,i}}\right)_{\parallel} + \left(\frac{E_{0,r}}{E_{0,i}}\right)_{\perp}\right)^2 \quad (50)$$

A formal definition for reflectance can finally be written from Equation 50 using Equation 38 and Equation 44. Reflectance is formally defined in Equation 51.

$$R = (r_{\parallel} + r_{\perp})^2 \quad (51)$$

Similarly, after canceling both *A* terms, Equation 48 can be simplified as shown in Equation 52.

$$T = \frac{I_t A \cos\theta_t}{I_i A \cos\theta_i} = \frac{I_t \cos\theta_t}{I_i \cos\theta_i} \quad (52)$$

Equation 52 can be further modified using Equation 46 as shown in Equation 53.

$$T = \frac{I_t \cos\theta_t}{I_i \cos\theta_i} = \frac{\frac{1}{2}v_{p,t}\epsilon_2 {E_{0,t}}^2 \cos\theta_t}{\frac{1}{2}v_{p,i}\epsilon_1 {E_{0,i}}^2 \cos\theta_i} = \frac{v_{p,t}\epsilon_2 {E_{0,t}}^2 \cos\theta_t}{v_{p,i}\epsilon_1 {E_{0,i}}^2 \cos\theta_i} \quad (53)$$

An additional physical relationship must be recognized in order to further simplify Equation 53. Magnetic permeability (μ) and electric permittivity are related to the phase velocity of an electromagnetic wave as shown in Equation 54 [23].

$$v_p = \frac{1}{\sqrt{\epsilon\mu}} \tag{54}$$

Assuming that both involved materials are non-magnetic ($\mu_1 = \mu_2 = \mu_0$, where μ_1 and μ_2 are the magnetic permeabilities of Region 1 and Region 2 respectively and μ_0 is the permeability constant), Equation 54 and Equation 2 can be used to rewrite Equation 53 as shown in Equation 55 and Equation 56.

$$T = \frac{v_{p,t}\epsilon_2 {E_{0,t}}^2 \cos\theta_t}{v_{p,i}\epsilon_1 {E_{0,i}}^2 \cos\theta_i} = \frac{\frac{n_2}{c\mu_0}{E_{0,t}}^2 \cos\theta_t}{\frac{n_1}{c\mu_0}{E_{0,i}}^2 \cos\theta_i} = \frac{n_2 {E_{0,t}}^2 \cos\theta_t}{n_1 {E_{0,i}}^2 \cos\theta_i} \tag{55}$$

$$T = \frac{n_2 \cos\theta_t}{n_1 \cos\theta_i}\left(\left(\frac{E_{0,t}}{E_{0,i}}\right)_{\parallel} + \left(\frac{E_{0,t}}{E_{0,i}}\right)_{\perp}\right)^2 \tag{56}$$

A formal definition for transmittance can finally be written from Equation 56 using Equation 39 and Equation 45. Transmittance is formally defined in Equation 57.

$$T = \frac{n_2 \cos\theta_t}{n_1 \cos\theta_i}(t_{\parallel} + t_{\perp})^2 \tag{57}$$

The International Commission on Illumination (CIE) and International Electrotechnical Commission (IEC) draw a distinction between the reflectance transmittance properties of a material and the reflectivity transmissivity properties of a material by specifying that the latter pair are properties of a thick sample of a given material. For thin materials, reflectance and transmittance can vary with the thickness of the material due to internal reflection effects. Reflectivity and transmissivity can therefore be formally defined as the limits of the reflectance and transmittance of a material as the sample thickness increases sufficiently to eliminate internal reflection effects. Thus, reflectivity and transmissivity are intrinsic properties of a material that must be specified in order to meaningfully compare the reflective and transmissive behaviors of different materials [28].

Appendix B: Azimuthal Angular Dependence Measurement Data

Experimental retroreflectivity measurement data for Sample 1, Sample 2, Sample 3, Sample 4, and Sample 5 (as described in Table 3) is included in Table 10, Table 11, Table 12, Table 13, and Table 14 respectively. Measurements were taken using a modified Delta LTL-X retroreflectometer and scaled according to the appropriate scaling factor (16:6).

Table 10: Azimuthal Angular Dependence Measurement Data (Sample 1)

	Azimuthal Angle: 0°	**Azimuthal Angle: 90°**	**Azimuthal Angle: 180°**
Measurements	**Retroreflectivity ($mcd/m^2/lux$)**	**Retroreflectivity ($mcd/m^2/lux$)**	**Retroreflectivity ($mcd/m^2/lux$)**
1	16	15	19
2	17	16	19
3	16	16	16
4	16	16	19
5	19	16	16
6	24	16	13
7	21	19	16
8	19	19	19
9	16	21	21
10	19	21	19
11	19	21	19
12	16	16	24
13	21	21	21
14	13	21	24
15	13	19	19
16	13	19	21
17	24	16	13
18	19	19	19
19	16	19	21
20	16	22	19
Average	**18**	**18**	**19**

Table 11: Azimuthal Angular Dependence Measurement Data (Sample 2)

	Azimuthal Angle: 0°	**Azimuthal Angle: 90°**	**Azimuthal Angle: 180°**
Measurements	**Retroreflectivity (mcd/m^2/lux)**	**Retroreflectivity (mcd/m^2/lux)**	**Retroreflectivity (mcd/m^2/lux)**
1	13	16	16
2	13	16	19
3	16	13	19
4	16	13	16
5	16	13	16
6	13	13	13
7	11	16	13
8	11	15	19
9	11	15	15
10	12	15	16
11	13	15	16
12	16	15	13
13	15	19	13
14	15	16	13
15	16	16	11
16	16	16	11
17	16	13	13
18	16	16	13
19	19	16	16
20	16	16	16
Average	**15**	**15**	**15**

Table 12: Azimuthal Angular Dependence Measurement Data (Sample 3)

	Azimuthal Angle: 0°	**Azimuthal Angle: 90°**	**Azimuthal Angle: 180°**
Measurements	**Retroreflectivity (mcd/m^2/lux)**	**Retroreflectivity (mcd/m^2/lux)**	**Retroreflectivity (mcd/m^2/lux)**
1	341	381	544
2	597	340	544
3	587	250	448
4	608	319	475
5	651	312	459
6	389	354	523
7	117	430	613
8	27	492	501
9	80	395	395
10	128	270	293
11	213	222	181
12	336	173	155
13	395	208	75
14	341	166	59
15	341	97	85
16	373	173	85
17	304	201	256
18	379	409	432
19	459	548	501
20	453	541	699
Average	**356**	**314**	**366**

Table 13: Azimuthal Angular Dependence Measurement Data (Sample 4)

	Azimuthal Angle: 0°	**Azimuthal Angle: 90°**	**Azimuthal Angle: 180°**
Measurements	**Retroreflectivity (mcd/m^2/lux)**	**Retroreflectivity (mcd/m^2/lux)**	**Retroreflectivity (mcd/m^2/lux)**
1	341	408	296
2	352	445	323
3	384	475	477
4	440	315	363
5	531	355	477
6	443	429	435
7	437	456	381
8	456	376	451
9	416	435	379
10	437	445	496
11	411	416	427
12	248	445	515
13	416	475	248
14	344	315	381
15	499	355	448
16	496	429	387
17	443	456	472
18	440	376	400
19	405	435	499
20	427	445	464
Average	**418**	**414**	**416**

Table 14: Azimuthal Angular Dependence Measurement Data (Sample 5)

	Azimuthal Angle: 0°	**Azimuthal Angle: 90°**	**Azimuthal Angle: 180°**
Measurements	**Retroreflectivity (mcd/m^2/lux)**	**Retroreflectivity (mcd/m^2/lux)**	**Retroreflectivity (mcd/m^2/lux)**
1	261	347	267
2	285	347	272
3	379	333	277
4	459	336	328
5	261	301	301
6	352	349	272
7	365	357	352
8	405	248	304
9	400	325	299
10	355	256	371
11	336	432	413
12	245	421	365
13	283	413	283
14	269	352	280
15	357	376	328
16	352	331	267
17	291	325	269
18	392	360	259
19	304	325	363
20	320	301	291
Average	**334**	**342**	**308**

Appendix C: Binder Reflectivity Measurement Data

Experimental illuminance measurement data for the mirror, white epoxy binder sample, and yellow epoxy binder sample is included in Table 15. Measurements were taken using a Dr. Meter LX1330B digital illuminance meter.

Table 15: Binder Reflectivity Measurement Data

		Polar Angle: 30°	**Polar Angle: 50°**	**Polar Angle: 70°**
	Dominant Incident Wavelength (nm)	**Illuminance (lux)**	**Illuminance (lux)**	**Illuminance (lux)**
Mirror	623	6.9	6.4	6.9
	534	9.9	9.5	10.0
	457	17.1	17.1	17.2
	395	1.3	1.3	1.3
White Binder	623	0.7	0.6	0.6
	534	1.0	0.9	0.9
	457	1.7	1.6	1.5
	395	0.1	0.1	0.1
Yellow Binder	623	0.6	0.5	0.7
	534	0.7	0.6	0.8
	457	1.2	1.1	1.3
	395	0.1	0.1	0.1

Appendix D: Machine Vision Imaging Measurement Data

Experimental average pixel intensity measurement data for the white roadway marking, yellow roadway marking, and black tar paper is included in Table 16. The images were captured using a JAI RM-6740CL CCD camera. In each grayscale image, the region corresponding to the imaged target was identified and spatially filtered using MathWorks MATLAB software. Average pixel intensity values for the identified region were then calculated.

Table 16: Machine Vision Imaging Measurement Data

		White Roadway Marking	**Yellow Roadway Marking**	**Black Tar Paper**
Optical Imager Polar Angle	**Light Source Polar Angle**	**Average Pixel Intensity of Target**	**Average Pixel Intensity of Target**	**Average Pixel Intensity of Target**
30	30	111	48	11
30	60	54	30	10
30	90	55	31	11
30	120	51	31	13
30	150	44	28	26
60	30	41	25	11
60	60	127	56	11
60	90	60	33	13
60	120	54	32	15
60	150	41	25	13
90	30	39	24	11
90	60	59	32	12
90	90	126	65	10
90	120	52	29	12
90	150	37	23	11

Captured images for the white and yellow roadway marking samples are shown in Figure 56 and Figure 57 respectively. All images were captured using the methodology described in Section 8.

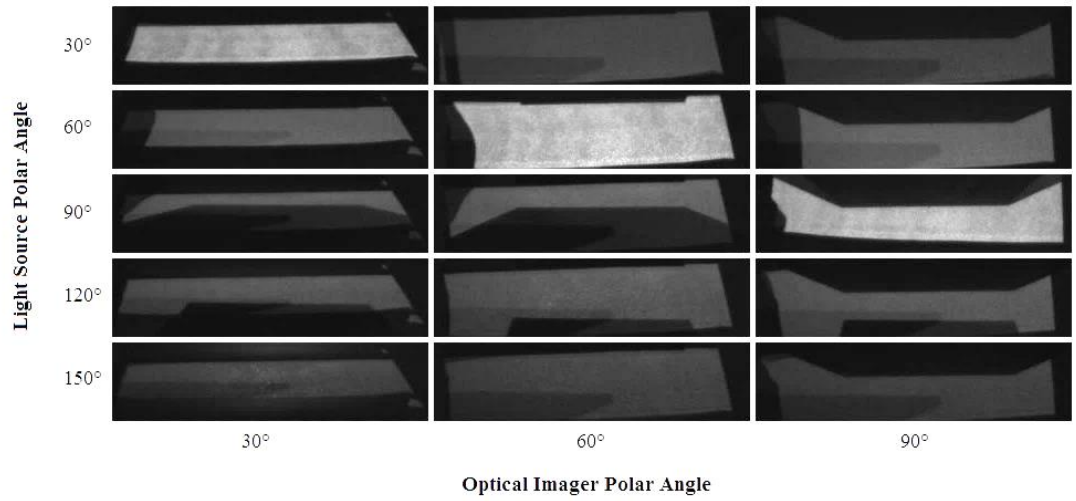

Figure 56: Machine vision imaging captured images (white roadway marking).

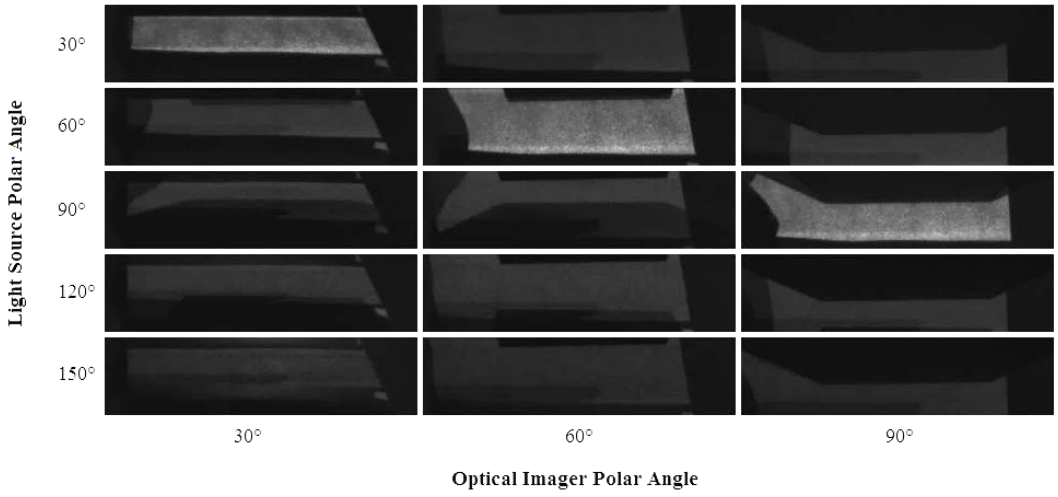

Figure 57: Machine vision imaging captured images (yellow roadway marking).

Vita

Anthony T. Konopka was born to Anthony J. and Cheryl L. Konopka in Hackettstown, New Jersey on March 27, 1994. He graduated from West Milford High School and matriculated at Lehigh University where he received the degree of Bachelor of Science in Electrical Engineering with Highest Honors in May of 2016. While at Lehigh, Mr. Konopka was also a recipient of the President's Scholar Award. During the Fall of 2014 and the Summer of 2015, he was engaged in work at Lutron Electronics Co., Coopersburg, Pennsylvania, where he completed multiple projects involving the design of electronics and optical systems. During the Summer and Fall of 2016, he was engaged in a research project at LimnTech Scientific Inc., Souderton, Pennsylvania, where his research involved machine vision systems and optical sensing. Mr. Konopka has accepted a position as a Senior Project Electrical Engineer at Lutron Electronics Co., Coopersburg, Pennsylvania.